APPLIED SCIENCES AND ENGINEERING

Water-powered, electronics-free dressings that electrically stimulate wounds for rapid wound closure

Rajaram Kaveti[1,2]†, Margaret A. Jakus[3]†, Henry Chen[2,4], Bhavya Jain[1,2], Darragh G. Kennedy[3], Elizabeth A. Caso[3], Navya Mishra[1,2], Nivesh Sharma[1,2], Baha Erim Uzunoğlu[1,2], Won Bae Han[5,6], Tae-Min Jang[5], Suk-Won Hwang[5,7,8], Georgios Theocharidis[9], Brandon J. Sumpio[9], Aristidis Veves[9], Samuel K. Sia[3]*, Amay J. Bandodkar[1,2,4]*

Chronic wounds affect ~2% of the U.S. population and increase risks of amputation and mortality. Unfortunately, treatments for such wounds are often expensive, complex, and only moderately effective. Electrotherapy represents a cost-effective treatment; however, its reliance on bulky equipment limits its clinical use. Here, we introduce water-powered, electronics-free dressings (WPEDs) that offer a unique solution to this issue. The WPED performs even under harsh conditions—situations wherein many present treatments fail. It uses a flexible, biocompatible magnesium-silver/silver chloride battery and a pair of stimulation electrodes; upon the addition of water, the battery creates a radial electric field. Experiments in diabetic mice confirm the WPED's ability to accelerate wound closure and promote healing by increasing epidermal thickness, modulating inflammation, and promoting angiogenesis. Across preclinical wound models, the WPED-treated group heals faster than the control with wound closure rates comparable to treatments requiring expensive biologics and/or complex electronics. The results demonstrate the WPED's potential as an effective and more practical wound treatment dressing.

INTRODUCTION

Chronic wounds are characterized by impaired healing and affect millions globally (*1*). These wounds result from a variety of factors, including prolonged exposure of skin to external pressure, venous and arterial insufficiency, peripheral neuropathy, diabetes mellitus, and surgical complications (*2*, *3*). The U.S. Centers for Medicare & Medicaid Services alone spends more than $28 billion annually to treat such wounds (*4*) and the expenditure is expected to grow for the foreseeable future due to the increasing number of individuals with diabetes, obesity, cancer, and other comorbidities (*5*, *6*).

Present products for treating chronic wounds include occlusive dressings (*7*), hydrogels (*8*), skin substitutes (*9*), and topical growth factors (*10*). While occlusive dressings, gauze, and hydrogels are relatively low-cost and user-friendly, they show limited effectiveness against complex chronic wounds. More advanced treatments such as skin substitutes and topical growth factors are still only moderately effective, at best achieving complete wound healing in ~50% of cases (*11*), while often costing well over $1000, and sometimes more than $20,000, per wound closure (*12*). Current research into biologics-based systems includes stem cell–loaded hydrogels (*13*–*15*), growth factor delivery systems (*16*–*21*), and multilayered scaffolds (*22*, *23*). However, stem cells and growth factors remain expensive and challenging to work with, and scaffolds can suffer from shrinkage and fail to recreate the heterogeneous skin environment (*24*). There is therefore a need to develop low-cost, highly effective treatments. In this context, electrotherapy, which involves the use of an external electrical field to drive wound closure, shows great promise (*25*–*28*) with recent examples illustrating low-cost, skin-friendly electrodes for efficient delivery of electrical stimulation to wounds (*29*, *30*). Preclinical and clinical studies show that electrotherapy leads to increased cell migration, venous blood flow, and cell proliferation, among other pro-healing effects resulting in rapid wound closure (*31*–*33*). However, achieving the best patient outcomes using this method requires daily treatment for several hours typically for weeks at a time (*34*). This places an exorbitant strain on the patients, as the stimulation electrodes are connected to bulky benchtop devices, restricting patient mobility for the duration of treatment and limiting the practical use of electrotherapy in wound care (*35*–*37*).

Emerging work in the area of battery-free, radio frequency (RF)–powered (*25*, *38*) and battery-powered wearable electronics enables the realization of miniaturized, smart dressings that support electrotherapy (*26*–*28*, *39*–*43*). However, battery-powered systems are still quite bulky and pose safety concerns when interfaced with the delicate wound. Battery-free, RF-powered platforms require that patients are in the vicinity of a transmitting antenna to wirelessly power the device, which restricts patient mobility. These systems also require meticulously designed transmission and receiving antennae and rely on expensive and bulky equipment such as RF amplifiers, function generators, and advanced impedance matching units (*44*, *45*). Moreover, the fragility of both battery-powered and battery-free electronics–based systems limit their use in body regions that bear high pressures and are prone to developing chronic wounds, such as the heel of the foot and the sacrum (*46*). Triboelectric nanogenerators offer an

[1]Department of Electrical and Computer Engineering, North Carolina State University, Raleigh, NC 27606, USA. [2]Center for Advanced Self-Powered Systems of Integrated Sensors and Technologies (ASSIST), North Carolina State University, Raleigh, NC 27606, USA. [3]Department of Biomedical Engineering, Columbia University, New York, NY 10027, USA. [4]Joint Department of Biomedical Engineering, North Carolina State University and University of North Carolina at Chapel Hill, Raleigh, NC 27606, USA. [5]KU-KIST Graduate School of Converging Science and Technology, Korea University, 145 Anam-ro, Seongbuk-gu, Seoul 02841, Republic of Korea. [6]George W. Woodruff School of Mechanical Engineering, Georgia Institute of Technology, Atlanta, GA 30332, USA. [7]Center for Biomaterials, Biomedical Research Institute, Korea Institute of Science and Technology (KIST), 5 Hwarang-ro 14-gil, Seongbuk-gu, Seoul 02792, Republic of Korea. [8]Department of Integrative Energy Engineering, Korea University, 145 Anam-ro, Seongbuk-gu, Seoul 02841, Republic of Korea. [9]Joslin-Beth Israel Deaconess Foot Center and The Rongxiang Xu, MD, Center for Regenerative Therapeutics, Beth Israel Deaconess Medical Center, Harvard Medical School, Boston, MA 02215, USA.
*Corresponding author. Email: ss2735@columbia.edu (S.K.S.); ajbandod@ncsu.edu (A.J.B.)
†These authors contributed equally to this work.

unconventional approach to delivering electrotherapy (*47*, *48*), though they generate an electrical field only when the participant is moving (*39*) or when interfaced with an external tethered linear motor (*49*). Beyond wound healing, electrotherapy systems also show promise in other areas of tissue regeneration, including cell modulation (*50*), nerve regeneration (*51*), and osteogenesis (*52*, *53*).

Here, we describe a water-powered, electronics-free dressing (WPED; Fig. 1A) that electrically stimulates the wound, leading to rates of wound closure comparable to those with expensive biologics- or electronics-based approaches (*27*, *28*, *49*, *54*–*58*) at a fraction of the cost (~$1 per dressing). The device includes a flexible, water-powered battery and a pair of thin-film stimulation electrodes

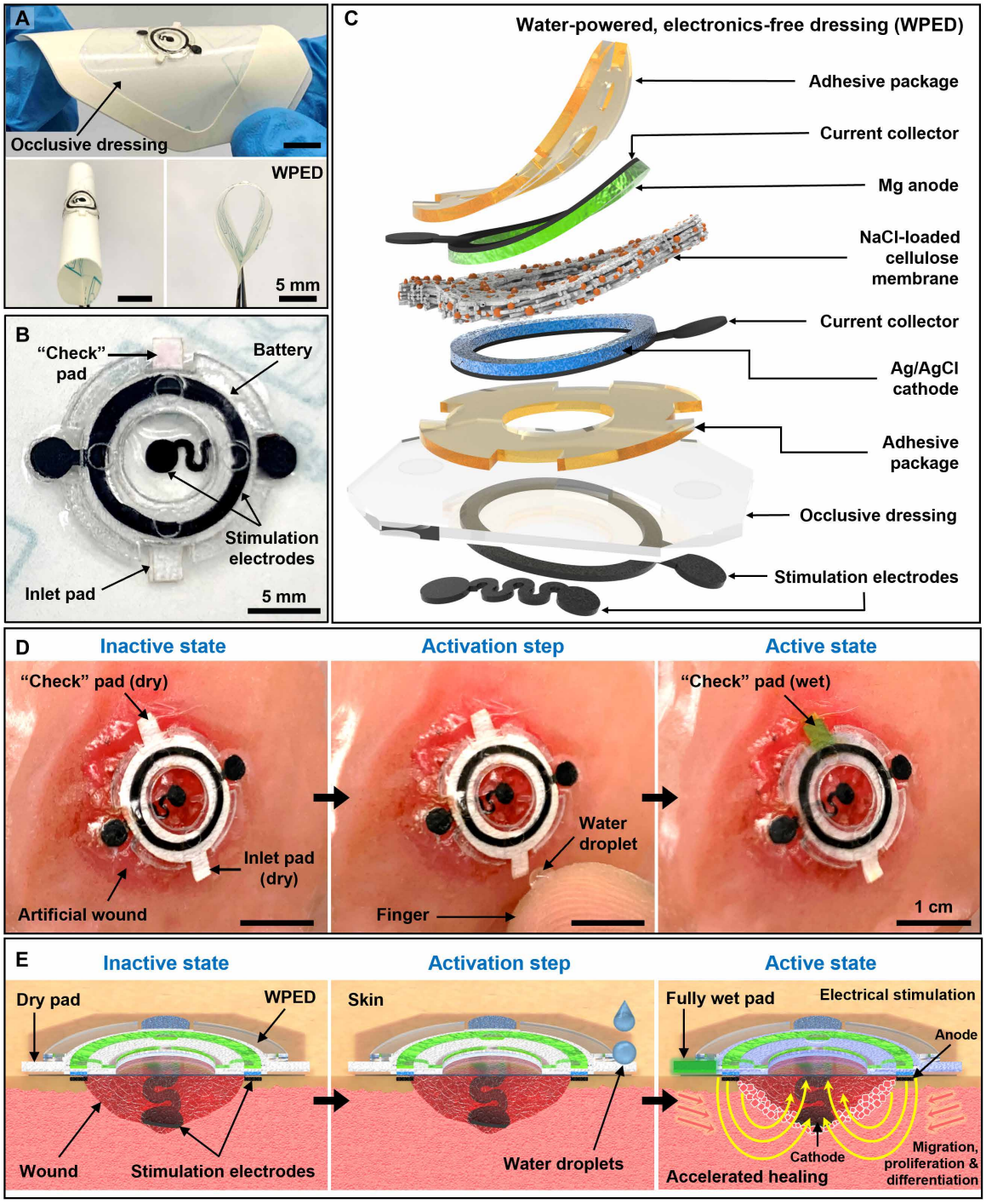

Fig. 1. Materials, design, and working principle of WPED. (**A**) Photographs of WPED illustrating its conformability. (**B**) Zoomed-in image of WPED showing the water-powered battery. (**C**) Exploded view schematic illustration of WPED showing the main components of the system. (**D**) Key steps involved in using WPED demonstrated with a dummy wound on the ball of a foot of a human participant. (**E**) Cross-sectional view illustrations showing the activation and working mechanism of WPED.

seamlessly integrated with a commercial dressing. The battery produces an electrical field across the stimulation electrodes when activated with water. Unlike present examples of electronics-based electrotherapy dressings, the water-powered dressings offer several hours of continuous stimulation with no restriction on patient mobility, robust performance (even under extreme temperatures, ambient humidity, and external pressures), and long shelf-life owing to their materials, design architecture, and working principle. Through rigorous benchtop and in vivo studies in diabetic mice, we demonstrate that the WPED offers an inexpensive yet highly effective wound treatment alternative to present approaches.

RESULTS

Working principle and key components of WPED

Figure 1A shows images of the lightweight, thin, flexible WPED. It involves a biocompatible magnesium-silver/silver chloride (Mg-Ag/AgCl) battery (area: 0.64 cm^2; weight: 47 mg; capacity: 0.4 mAh) affixed to the nonadhesive side of a commercial bandage (Tegaderm) and a pair of carbon-based stimulation electrodes on the adhesive side (facing the wound). The complete system (battery + electrodes + Tegaderm) is light (290 mg, only ~20% heavier than Tegaderm) and highly flexible for conformal attachment on curvilinear body parts such as toes (fig. S1A). Tables S1 and S2 show the specifications and performance metrics for WPED, respectively. A degradation test performed by continuously incubating the carbon-based stimulation electrodes in artificial wound fluid (AWF) at 37°C for 7 days shows negligible impact on their electrical properties (resistance increment of <10%) indicating their inert electrical behavior and suitability for interfacing with wounds (fig. S1B).

Figure 1B shows a close-up view of WPED, while Fig. 1C illustrates a schematic representation of the key components of the dressing. The water-powered battery, based on our previous work (*59*), is ring-shaped for easy visual assessment of the wound. The battery includes a magnesium (Mg) anode and a silver/silver chloride (Ag/AgCl) cathode with a dry cellulose separator impregnated with sodium chloride (NaCl). The battery is packaged within a polyethylene terephthalate film and is in an open-circuit state (i.e., inactive state) when the separator is dry. The separator includes an inlet pad where the user introduces water to activate the battery and a "check" pad to visually indicate complete hydration of the separator and successful activation of the battery. The working principle of the "check" pad is presented in fig. S2A and described in our previous work (*60*). Upon activation, the battery produces a voltage (~1.5 V) across the pair of stimulation electrodes which include a central disk electrode connected to the anode (Mg; negative electrode) and an outer ring electrode attached to the cathode (Ag/AgCl; positive electrode). Such a configuration ensures a radial electrical field pointing to the wound center in line with the endogenous electrical field, critical for promoting healing (*25*). Key attributes of using the water-powered battery over conventional thin-film batteries include the ability to offer on-demand electrotherapy, simplicity, and no reliance on toxic electrolytes, as is the case with conventional batteries. Figure 1D and movie S1 demonstrate the key steps involved and the ease of using these standalone dressings. The user simply applies the dressing to the wound and touches the inlet pad with a moist fingertip to activate the dormant battery until the "check" pad changes color, indicating successful activation. Figure 1E shows the working principle of the dressing.

Eventual evaporation of the water from the separator leads to an increase in the internal resistance of the battery culminating in its deactivation when the separator is nearly dry. An advanced version of the WPED includes a humidity indicator (Humidity Detection Test Paper, Bartovation, USA) affixed to the inlet pad to provide a real-time visual indication of the moisture content of the separator (fig. S2B). The humidity indicator changes its color from blue to light pink when water is added to the inlet pad. The indicator returns to its blue color when the separator dries due to water evaporation. As shown in fig. S2B, the user can simply look at the color of the humidity indicator to gauge the real-time status of the WPED's ability to deliver electrical stimulation. Advanced versions of WPED could also be developed in the future that include additional electrochromic displays (*61*) that provide a colorimetric indication of the instantaneous output voltage of the WPED for a more accurate assessment of its real-time ability to electrically stimulate wounds.

Three-dimensional morphable stimulation electrodes for deep and complex wounds

Wound beds can have complex, deep, and irregularly shaped three-dimensional (3D) contours (*56*). Integration of the WPED with such wounds requires stimulation electrode designs with mechanical features capable of conformally mounting on such 3D-contoured soft tissues (*3*, *62*). In this context, kirigami-inspired designs offer a unique solution due to their ability to assume 3D morphable structures and accommodate large, out-of-plane deformations (*63*, *64*). The fabrication processes involved in realizing WPED allow the development of advanced versions of the therapy platform with kirigami-inspired 3D morphable stimulation electrodes as shown in Fig. 2A.

The device includes a self-similar serpentine outer electrode (OE) and spiral-shaped inner electrode (IE). Figure 2B shows the ability of the kirigami-based electrodes to expand in 3D under varying degrees of strains. Figure 2C shows corresponding simulation results capturing the stress generated within the stimulation electrodes. The kirigami electrodes exhibit elastic deformation with uniform stress distribution across the electrode lengths resulting in a stable mechanical deformation. Electrical characterization of the stimulation electrodes reveals stable resistance for both electrodes with only ~14 and ~13% increase in resistance for the OE under 100% biaxial strain (ultimate elongation of ~130%) and IE under ~2500% uniaxial strain (ultimate elongation of ~3300%), respectively, which is comparable to previous studies (*65*). The sharp rise in the resistance beyond these strains could be attributed to microcracks generated in the carbon layer.

The configurable nature of the kirigami-based stimulation electrodes allows the OE to expand laterally for mounting it along the periphery and the spiral-shaped IE to unwind and interface with the center of wounds with various complex shapes, sizes, and depths, as shown in Fig. 2 (E and F), fig. S3, and movie S2.

Electrical characterization of WPED

Complete hydration of the separator is important to ensure the battery attains maximum possible capacity which is critical for delivering long durations of electrical stimulation. Figure 3A shows the effect of the total volume of water applied on the areal capacity of the battery. Increasing the amount of water introduced into the battery leads to an increase in the ionic conductivity of the separator and a decrease in the battery's internal resistance resulting in increasing

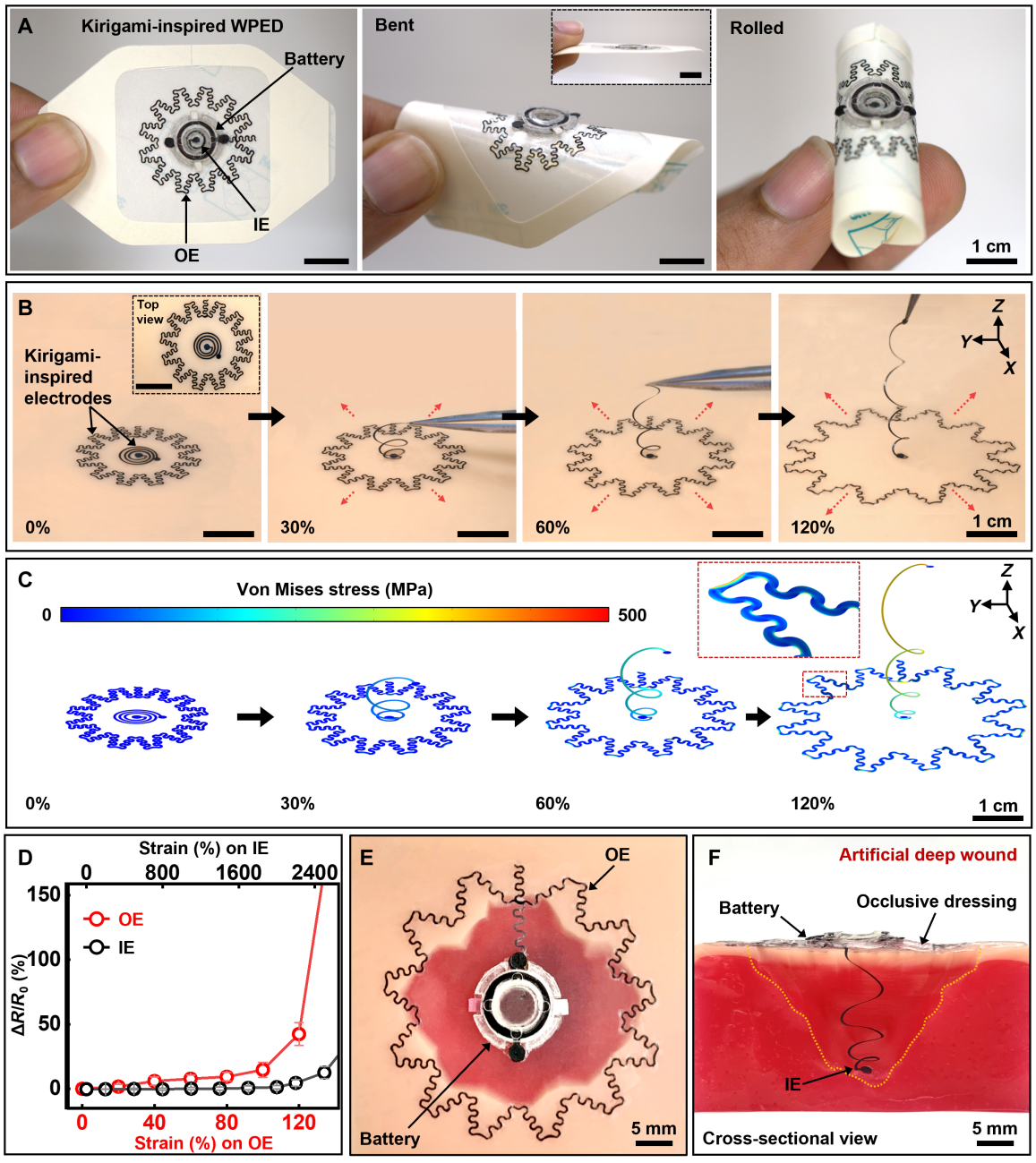

Fig. 2. Kirigami-inspired WPED for complex, deep wounds. (**A**) Photographic images of WPED with kirigami-inspired stimulation electrodes (left), device under bent (center), and rolled (right) state. Inset shows the side view of WPED. Scale bar, 1 cm. (**B**) Photographs of kirigami-based stimulation electrodes under 0, 30, 60, and 120% biaxial and uniaxial stretching for outer and inner electrodes, respectively. Inset shows the top view of electrodes. Scale bar, 1 cm. (**C**) Corresponding mechanical finite element analysis (FEA) results for kirigami-based stimulation electrodes. (**D**) Relative change in the electrical resistance of kirigami electrodes as a function of strain. $n = 3$. A photograph showing the top view (**E**) and a photograph showing the cross-sectional view (**F**) of kirigami-based WPED interfaced with an artificial deep wound with complex shape and contours (diameter: 3.2 cm; depth: 2.1 cm). All data are means ± SD.

areal capacity. The areal capacity peaks at ~4.5 mAh/cm^2 for ~20 μl/cm^2 of water followed by a small decrease for batteries exposed to higher quantities of water. This decrement in the battery capacity can be attributed to the accelerated oxide formation on the Mg anode leading to an increase in the battery's internal resistance as reported by us previously (*59*). Figure S4 shows the importance of the "check" pad to ascertain the appropriate activation of the battery. The dressing includes a 0.64-cm^2 battery suitable for treating 1-cm diameter wounds as described later. The images clearly show that the "check" pad changes color only when the minimum required quantity of water (~20 μl/cm^2) is applied to the battery. Figure 3B shows that the capacity of the battery is negligibly affected by the source of the water and that it can be powered even using the wound exudate, thus opening the possibility for developing a dressing that

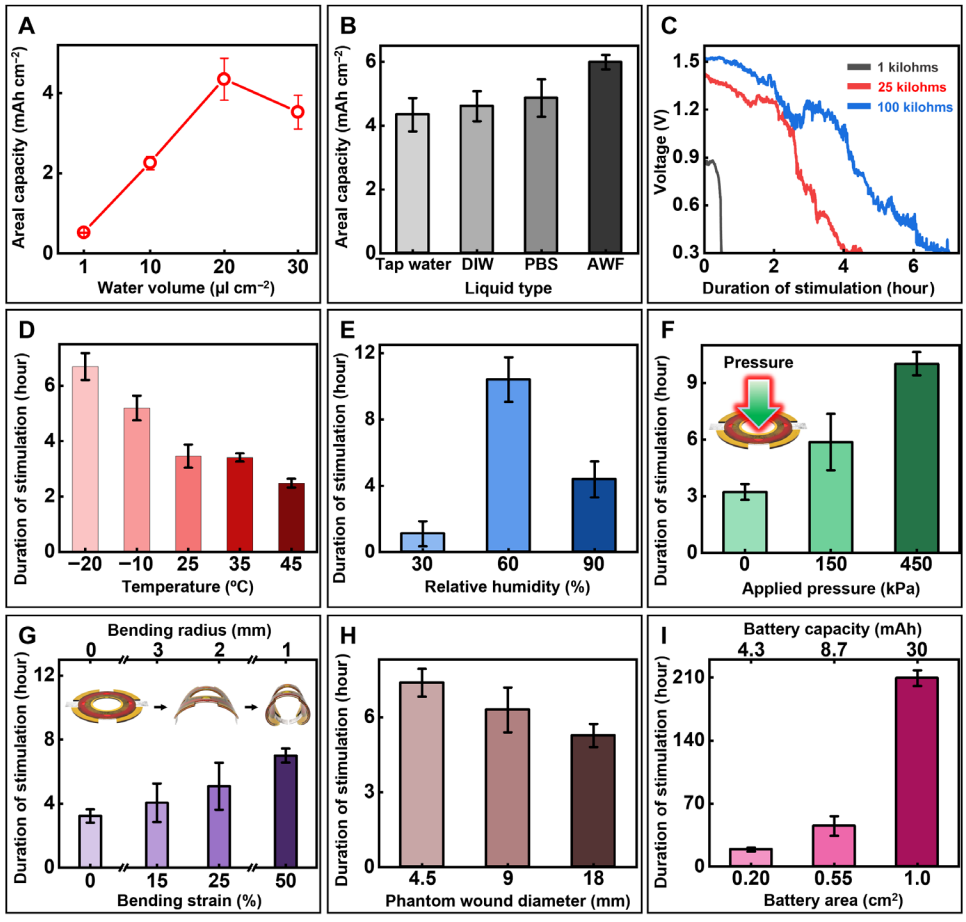

Fig. 3. In vitro electrical characterization of WPED. (**A**) Battery capacity as a function of the volume of water added to the separator; discharge current: 1 mA/cm^2. (**B**) Effect of type of fluid used to activate the battery on capacity; discharge current: 1 mA/cm^2. DIW, deionized water; PBS, phosphate-buffered saline, pH 7; AWF, artificial wound fluid. (**C**) Duration of stimulation for different loads simulating different stages of wound healing. Effect of (**D**) temperature, (**E**) ambient humidity, (**F**) applied pressure, and (**G**) bending stress on duration of stimulation. (**H**) Duration of stimulation offered by WPED of fixed battery capacity (0.4 mAh) for treating wounds of different diameters. (**I**) Effect of battery capacity on duration of stimulation for treating wounds of fixed size. $n = 4$. (D) to (G) WPED applied to a load resistance (25 kilohms) simulating average wound resistance per fig. S3A. (H) and (I) Phantom wounds were created using chicken breasts with a diameter of 2.5 cm and a thickness of 2 cm. All data are means ± SD.

harvests local wound exudate to power the electrotherapy system. The AWF is prepared on the basis of previous work (*66*, *67*).

The duration of stimulation offered by the dressing also depends on the impedance of the wound which changes as the wound heals (*27*, *68*). Figure S5A shows daily wound impedances (wound size: 1-cm diameter) in male diabetic (db/db) mice (age: 11 to 13 weeks; $n = 6$) widely used for studying diabetic foot ulcer, a type of chronic wound (*28*, *49*, *56*–*58*, *67*). Wound impedance is measured by applying a pair of carbon electrodes (same as that used for stimulation) to the wound and interfacing it with an electrochemical impedance analyzer. Figure S5B exhibits an image of the experimental setup. The impedance gradually increases from 10 to 60 kilohms from the day of injury to full recovery (by day 15) consistent with previous studies (*27*). In vitro characterization of WPED involves connecting the stimulation electrodes across a resistor of varying resistance (to simulate wound status at different stages of healing), applying water to power the dressing, and recording the voltage across the resistor. All experiments include dressings composed of a 0.64-cm^2 battery connected to a central disk electrode (diameter: 2 mm) and outer ring electrode (outer diameter: 9 mm; inner diameter: 7.4 mm) designed to treat a 1-cm diameter wound (Fig. 1, A and B) unless otherwise noted. The results obtained with such stimulation electrodes are applicable to the kirigami-based system (Fig. 2) as well since the performance of the WPED does not depend on the design of the stimulation electrodes.

Several prior studies show that daily treatment of electrical stimulation ranging from 15 min to 6 hours can expedite wound healing (table S3). Moreover, these studies show that a wide range of electrical stimulation parameters (amplitudes, DC/AC, and duration of stimulation) have similar effects on wound healing. Separately, studies reveal that a minimum electrical field strength of 100 mV/mm is necessary to support pro-healing processes and expedite wound closure (*69*, *70*). These studies indicate that even a time-varying electrical field (as is the case in WPED) will promote healing as long as the field strength is greater than 100 mV/mm. We therefore define the duration of stimulation for WPED as the duration over which the WPED offers an electrical field strength of at least 100 mV/mm. Figure 3C shows that the duration of stimulation varies from 0.5 to

>7 hours depending on the wound impedance. Figure S5C shows the reproducible performance of WPED as a function of wound impedance. The dressing attains an initial output voltage of 1.5 V which gradually decreases until it reaches 0 V. The WPED's maximum voltage (1.5 V) is consistent with previous reports, where stimulating voltages ranging from 1 to 6 V have been reported. (*25, 26, 28, 29*). Unlike previous examples of electronics-based electrotherapy systems that produce a constant electrical field for a predetermined period of time, WPED generates a time-varying electrical field with a duration of stimulation dependent on the wound impedance. Advanced versions of WPED could include a preprogrammed voltage regulator to stabilize its output voltage. Nevertheless, it delivers long durations of stimulation (at least ~0.5 hours) irrespective of the wound impedance, which is critical for facilitating healing as reported previously (*71*, *72*) and as described later in in vivo studies.

The WPED with a 0.4-mAh battery offers ≥3.5-hour stimulation at temperatures up to 35°C (Fig. 3D). Investigation of the dressing's ability to deliver electrical stimulation at extreme temperatures (<0° and >35°C) reveals that the duration of stimulation decreases only by ~1 hour for elevated temperatures (up to 45°C) due to higher rates of water evaporation. On the other hand, the supersaturated salt electrolyte remains in the liquid state at subzero temperatures, ensuring the functioning of the battery even at such low temperatures. The reduced rates of evaporation at these temperatures facilitate the delivery of a substantially higher duration of stimulation. These results highlight the dressing's ability to perform even under harsh conditions wherein conventional lithium and alkaline battery–powered dressings face deterioration, thus opening possibilities for offering effective wound treatments in extreme weather conditions. The rate of water evaporation at higher temperatures could be minimized by developing separators using hygroscopic polymers that tightly bind water molecules (*73*, *74*). Under arid conditions [30% relative humidity (RH)], the dressing offers stimulation for ~1 hour which increases to ~10.5 hours at 60% RH and then falls to ~4.5 hours at 90% RH (Fig. 3E). Figure S5D exhibits typical evolution of voltage as a function of time under different ambient humidity levels. These results are expected as increased humidity levels reduce water evaporation while very high humidity levels accelerate Mg oxidation leading to a lower duration of stimulation and increased variability in voltage due to excessive generation of hydrogen gas bubbles at the electrode-separator interface. These issues can be alleviated by using Mg alloys, special electrode coatings, and/or additives to the separator to reduce corrosion and hydrogen gas production (*75*, *76*). The duration of stimulation can be extended by nearly six times by preloading glycerol in the separator which acts as a humectant and reduces water evaporation from the separator (fig. S5E). Such modifications to the WPED can be especially beneficial to its performance in low-humidity settings. While these studies show that the performance of the WPED depends on ambient temperature and humidity, the results reveal that WPED offers hours-long stimulation irrespective of changes in these factors.

Chronic wounds often form at the foot or sacrum, areas that experience high external pressure loads (*77*–*79*). Figure 3F shows the performance of the dressing when subjected to external pressures in the range typically experienced by these body parts (0 to 450 kPa) (*78*). The duration of stimulation increases with pressure possibly due to reduced separation between the anode and cathode resulting in lower internal battery resistance and thus lower energy loss. Figure 3G illustrates the effect of bending stress on the dressing. The bending radii are selected to emulate conditions when the dressing is applied to curved surfaces (e.g., toes). A trend similar to Fig. 3F is recorded for such bending stresses. Figure S5F illustrates the effect of bending strain on the battery's output voltage. The data reveal that battery voltage decreases by only ~11% when the dressing is subjected to a bending strain of 100% (bending radius: 0.5 mm). Results in Fig. 3 (F and G) are quite interesting as they reveal that the dressing performs robustly for several hours even when continuously subjected to extremely high pressures (450 kPa) and bending stress (bending radius: 0.5 mm), unlike the expected performance from wireless electronics-based devices. The data reported in Fig. 3 (A to G) and fig. S5 are acquired by interfacing the WPED with a resistor (25 kilohms) to mimic average wound impedance.

The effect of wound size and battery capacity is investigated by applying WPED to a phantom wound (chicken breast; fig. S6A). Figure 3H shows that the duration of stimulation reduces by only 30% as the wound size increases fourfold. Figure S6B exhibits representative voltage versus duration of stimulation plots, while fig. S6C and fig. S6D illustrate the Nyquist plots and impedances for the three sizes of the phantom wounds studied in this experiment. Here, the battery (capacity: 0.4 mAh; area: 0.64 cm^2) and the central disk stimulation electrode (diameter: 2 mm) are maintained for all wound sizes, while the diameter of the ring electrode is matched with that of the wound. Results obtained while investigating the effect of battery size (and hence its capacity) on stimulation performance appear in Fig. 3I. A clear increase in duration of stimulation for a fixed wound size (diameter: 1 cm) is recorded as a function of battery area and capacity, demonstrating the ability of WPED to offer uninterrupted, multiday electrotherapy treatment. Furthermore, the dry nature of the batteries offers long shelf life; when tested after 7 months from the time of fabrication, the batteries show an average discharge capacity of 0.39 mAh which represents a 2.5% reduction in the capacity when compared to that of a freshly fabricated battery (0.4 mAh) (fig. S7). The small decrease in the battery capacity can be attributed to the formation of an oxide layer on the Mg surface during storage and can be minimized with tight vacuum-sealed packaging. The systematic experiments described in Fig. 3 and figs. S5 to S7 clearly demonstrate the potential of WPED to offer reliable, wound-specific electrotherapy treatment under conditions simulating real-life scenarios in a completely untethered and unencumbered fashion.

Finite element analysis studies

A 3D finite element analysis (FEA)–based wound-on-skin model allows spatial simulation of the electric field distribution around the wound site (*25*). The disk electrode is positioned on the adipose tissue, while the OE is placed on the dermis, replicating in vivo conditions. This setup allows the electric field to permeate the dermis and fortify the endogenous electric field, facilitating wound healing. The directional electric field, originating from the custom-designed electrical stimulation electrodes, creates an inward DC flow from the healthy site toward the center of the wound, mimicking naturally occurring endogenous wound currents (*80*). Figure 4A shows the spatial potential distribution for a wound (diameter: 1 cm). A peak electric field strength of ~530 mV/mm is produced near the central disk electrode which attenuates to ~100 mV/mm near the inner edge of the ring electrode (Fig. 4B). Such electrical field strengths are recognized as sufficient to induce migration of human keratinocyte cells and modulate cell behavior, including cell-cell junctions, cell division orientation, and cell migration trajectories

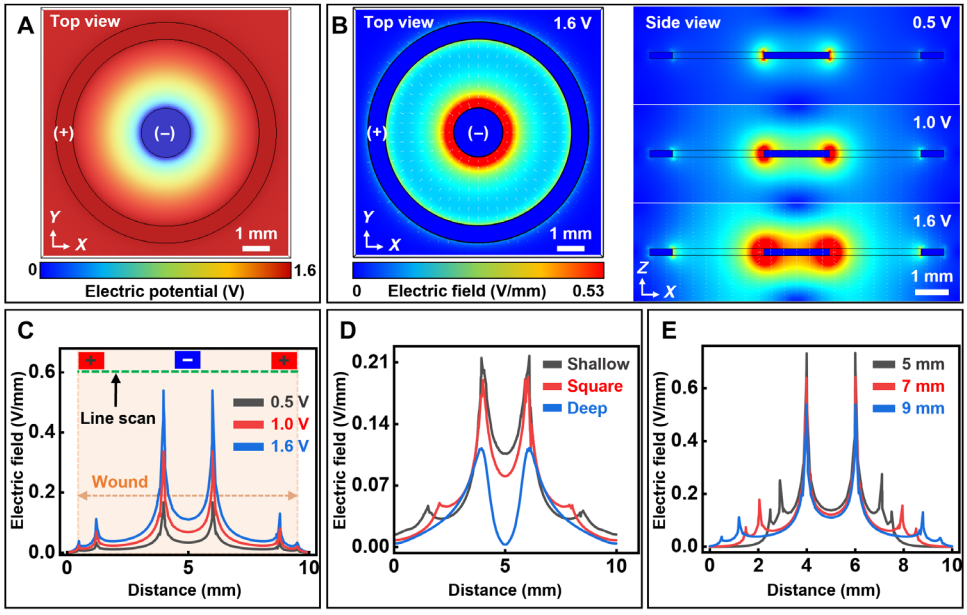

Fig. 4. Finite element analysis studies. (**A**) Electric potential distribution profile between the two stimulation electrodes with a battery output voltage of 1.6 V. (**B**) Top (left) and side (right) view of the electric field distribution at the wound site when treated with a WPED offering a voltage of 0.5, 1.0, 1.6 V. FEA simulation results showing electric field distribution profile across the wound length for different (**C**) applied voltages for a wound (diameter: 1 cm), (**D**) wound shapes, and (**E**) wound diameters.

(galvanostatic or electrotactic) (*69*, *81*, *82*) necessary to promote wound closure (*28*, *83*, *84*). Moreover, this distribution aligns with the effective DC electric field intensity known to enhance dorsal root ganglion neurite outgrowth, stimulate neurotrophic factors released by Schwann cells, and induce PC12 cell differentiation, as reported in previous studies (*85*–*87*). The electric field strength and distribution are influenced by the output voltage of the battery (Fig. 4C and fig. S8), wound shape (Fig. 4D and fig. S9), and wound size (Fig. 4E and fig. S10). The WPED can be easily adapted to treat deep wounds with narrow openings (e.g., puncture wounds) as demonstrated in fig. S11. Here, the two stimulation electrodes are mounted on either side of the wound to generate an electrical field across the wound. Such configuration for placing stimulation electrodes is widely used in several clinical settings (*88*). In the case of deep wounds, the electric field substantially diminishes when electrodes are positioned at the center and the periphery of the wound. Kirigami-inspired electrodes (Fig. 2 and fig. S3) may offer enhanced spatial electrical field strength and distribution while enabling improved conformal attachment to treat such wounds.

Evaluation of WPED in a diabetic mouse wound model

Before testing in vivo, the biocompatibility of WPED was evaluated using NIH/3T3 mouse fibroblasts cultured with standard media (fig. S12A) or standard media conditioned with the dressing (fig. S12B) for 72 hours. Quantification of live/dead staining at 72 hours reveals no substantial difference between the two groups (fig. S12C), confirming the dressing's biocompatibility.

Prior studies reveal that electrical stimulation accelerates migration in many cell types, including keratinocytes, fibroblasts, and macrophages (*89*). However, when tested in an in vitro scratch assay (fig. S13A), WPED slowed the migration of NIH/3T3 mouse fibroblasts (fig. S13B). Studies show that electrical stimulation can cause NIH/3T3 mouse fibroblasts to contract and develop larger focal adhesions (*90*). Separately, studies reveal that focal adhesion size causes a decrease in cell migration speed above a certain threshold (*91*). Figure S13C exhibits representative microscopic images of cells after receiving electrical stimulation for 24 hours via WPED (control: no electrical stimulation). A clear contraction in cell morphology is observed in cells that received electrical stimulation which could correlate with an increase in focal adhesion size and thus decreased migration speed. The exact mechanism by which electrical stimulation accelerates healing is still being actively investigated (*92*), and in vitro testing does not wholly recreate the in vivo environment. Given the pro-healing results in vivo (discussed later), it is likely that the effects of electrical stimulation are due to a combination of cellular processes, such as an up-regulation of angiogenic factors and other growth factors (*93*, *94*) that cannot be captured in a scratch test. The WPED's mechanism for promoting wound closure needs further investigation which could be achieved through systematic transcriptomic and proteomic analyses of the wound tissue (*95*).

Investigation of WPED in a wound closure diabetic (db/db) mouse model reveals its ability to accelerate wound closure. Wounds in these animals heal through a combination of epithelialization and contraction (*96*) and several studies leverage this model to study wound healing as it recapitulates wound repair impairment of human diabetic ulcers (*97*–*100*). Experiments involve creating a full-thickness excisional dermal wound (diameter: 1 cm) on the dorsum of each mouse (Fig. 5A, left) followed by covering it with the WPED ("Stim"; $n = 8$) as shown in Fig. 5A (right). Next, applying water to the battery initiates electrotherapy. The animal studies involve WPED design, as shown in Fig. 1, because of the simple, circular, and shallow nature of the wounds. Figure 5B shows infrared (IR) images of a mouse before and after activation of the WPED revealing that the electrical field generated by the dressing does not cause any measurable temperature variations in the adjacent tissue which is

important to avoid any thermally induced damage to the wound. Daily replacement and activation of the dressing over a period of 11 days after injury ensure sustained electrotherapy treatment. Such diurnal treatment is similar to the recommended treatment for becaplermin (U.S. Food and Drug Administration–approved product for diabetic foot ulcers) (*101*, *102*). Moreover, exchanging the WPED is fast, taking <1 min (movie S1), which is comparable to replacing conventional dressings. Additional studies involving animals treated with inactive dressing ("Sham"; no activation of the battery with water; $n = 8$) and occlusive dressing ("Control"; Tegaderm-only; $n = 7$) enable deconvolution of the effects of electrotherapy on wound closure from those due to material and geometric features of the stimulation electrodes and Tegaderm.

Representative images of wounds in three randomly selected mice each belonging to the three treatment groups captured on days 0, 3, 6, and 11 after injury appear in Fig. 5C. Figure 5D provides the longitudinal evolution of wound size for all animals in each group. Investigation of these results reveals that the Stim group displays substantially increased rates of wound closure beginning day 4 after injury compared to other groups. More specifically by day 11, 75% of wounds in the Stim group fully closed compared to 12.5 and 0% in the Sham and Control groups, respectively. Extended assessment beyond day 11 reveals that 88% of wounds in the Stim group completely close by day 13, while only 50 and 28% of wounds in the Sham and Control groups close at this time point. Overall, the animals that receive WPED treatment show 1.23× faster closure of wounds by day 11 as compared to other groups (Fig. 5E). The wound closure rate offered by these low-cost, easy-to-use dressings is 1.2× faster than becaplermin (*54*, *55*) and is comparable to wound closure rates reported in the literature (*27*, *28*, *49*, *56*–*58*) that rely on expensive biologics and/or electronics (table S4). The higher wound closure rates observed in the Sham group compared to the Control group can possibly be attributed to the stimulation electrodes serving as anchoring structures for migrating cells to adhere to, similar to the role many scaffolds play in wound healing (*103*–*107*). Figure 5F and fig. S14 exhibit representative movement profiles and total average distance traveled, respectively, by mice in the three groups. Movie S3

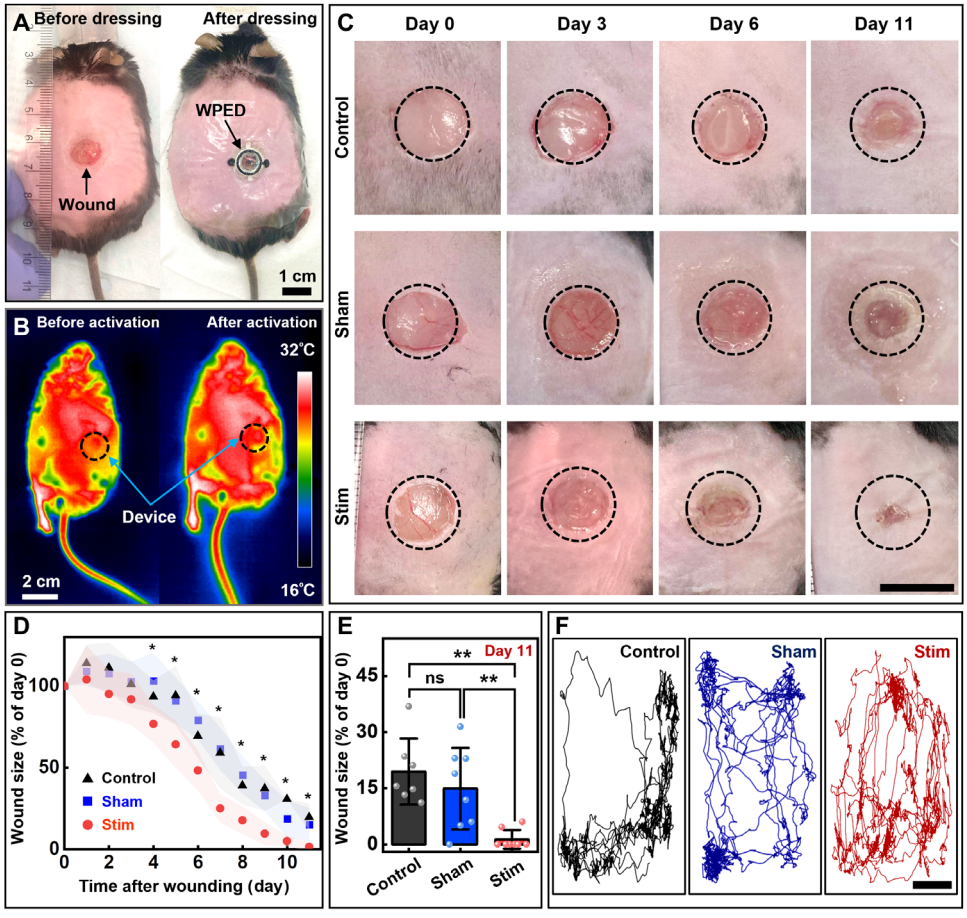

Fig. 5. In vivo evaluation of WPED in db/db mice. (**A**) Representative image of a db/db mouse wound before (left) and after (right) applying WPED. (**B**) Infrared images of a mouse wearing WPED before (left) and 5 min after (right) activation. (**C**) Representative macroscopic views of wounds on days 0, 3, 6, and 11 for the Control, Sham, and Stim groups. Scale bar, 10 mm. (**D**) Relative size of the wounds over time for the three groups. $n = 8$ for Sham and Stim. $n = 7$ for Control. A two-way analysis of variance (ANOVA) with multiple comparisons was performed, comparing the Sham and Control means with the Stim mean. $^*P < 0.05$ for both comparisons. (**E**) Wound closure on day 11. Tukey's multiple comparisons test was performed. $^{**}P < 0.01$ for both comparisons. ns, not significant. (**F**) Representative movement trajectories of individual Control, Sham, and Stim mice over 10 min. Scale bar, 5 mm.

shows a freely moving mouse wearing WPED. These results reveal that the WPED does not impede animal mobility in any way owing to its conformal, lightweight nature.

Histological analysis of the wounds further confirms the ability of the WPED to stimulate wound healing beyond simply accelerating closure. Hematoxylin and eosin (H&E) staining (Fig. 6A) and Masson's trichrome staining (MTS) (Fig. 6B) performed on tissue samples collected 13 days after injury reveal that the epidermis is 43 and 72% thicker ($P < 0.0001$) in the Stim group compared with the Sham and Control groups, respectively, with no notable difference between the epidermal thickness in the Sham and Control groups (Fig. 6C). Figure 6B shows MTS from the three groups; analysis

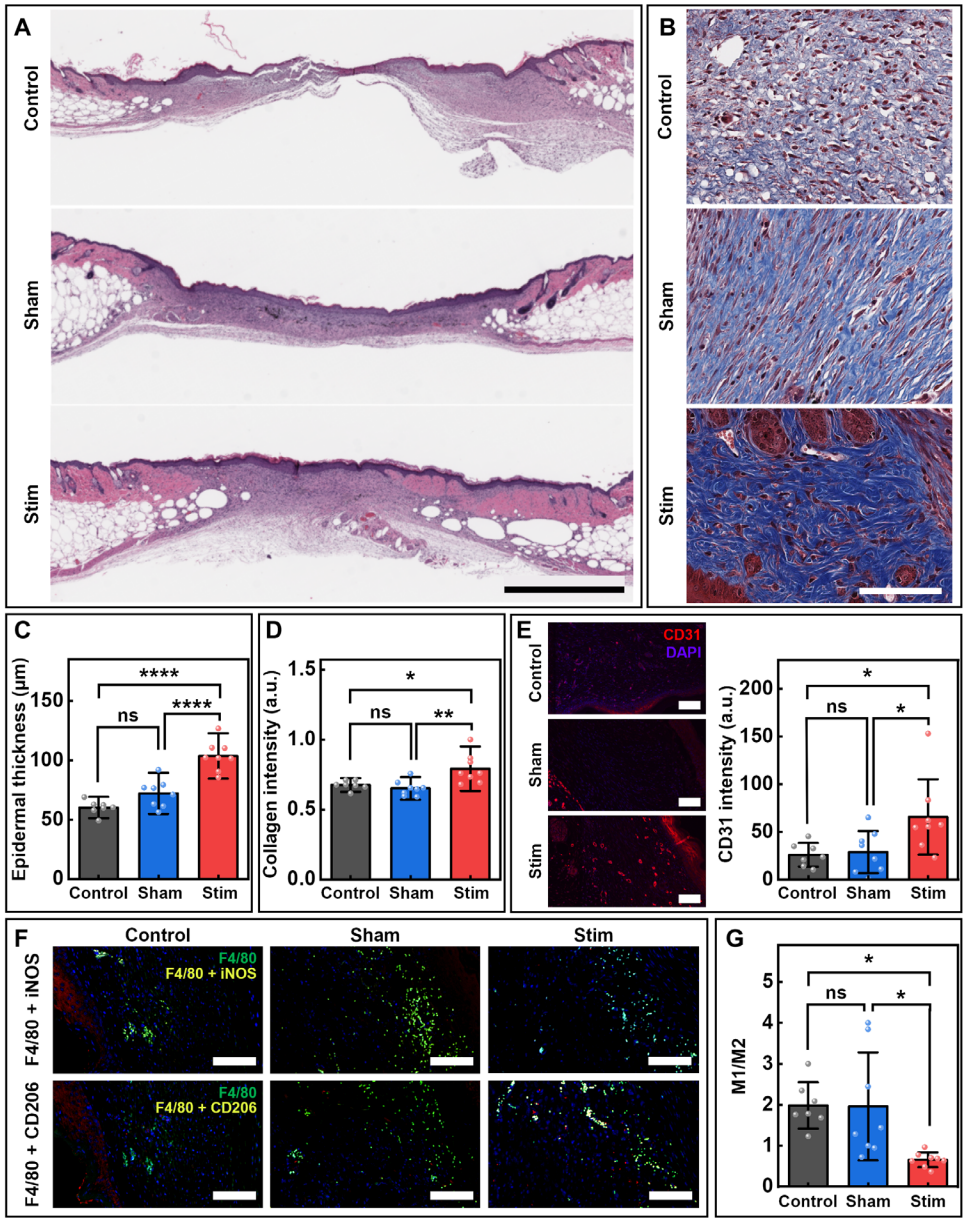

Fig. 6. Histological studies of wounds treated with WPED. (**A**) Representative cross-sectional images of wounds with hematoxylin and eosin stains for the Control, Sham, and Stim mice 13 days after wounding. Scale bar, 1 mm. (**B**) Representative cross-sectional Masson's trichrome stains of the center of the wounds for the Control, Sham, and Stim mice 13 days after wounding. Scale bar, 100 μm. (**C**) Quantitative comparison of the epidermal thickness of the Control, Sham, and Stim wounds. Ordinary one-way ANOVA with multiple comparisons was performed. ****$P < 0.0001$ for Control versus Stim and for Sham versus Stim. (**D**) Quantitative comparison of collagen intensity of the Control, Sham, and Stim wounds. Tukey's multiple comparisons test was performed. *$P < 0.05$ for Control versus Stim, **$P < 0.01$ for Sham versus Stim. (**E**) Immunofluorescence staining for CD31 (red) and DAPI (blue) in tissue from the Control, Sham, and Stim wounds (left). Scale bars, 100 μm. Quantification of CD31 intensity (right). Ordinary one-way ANOVA with multiple comparisons was performed. *$P < 0.05$ for Control versus Stim and for Sham versus Stim. (**F**) Immunofluorescence staining for F4/80 (green) and iNOS (red) for the Control, Sham, and Stim wounds (top row). Immunofluorescence staining for F4/80 (green) and CD206 (red) for the Control, Sham, and Stim wounds (bottom row). Double staining appears yellow. Scale bars, 100 μm. (**G**) Quantification of M1/M2 macrophage ratio of the Control, Sham, and Stim wounds. Tukey's multiple comparisons test was performed. *$P < 0.05$ for Control versus Stim and for Sham versus Stim. a.u., arbitrary units.

affirms increased collagen intensity in the Stim group as compared with the Sham and Control groups ($P < 0.01$) (Fig. 6D).

Epidermal regeneration is a central aspect of re-epithelialization, as the healthy epidermis acts as a barrier against pathogens and prevents fluid loss (*108*, *109*). Collagen is a main component of the extracellular matrix and contributes to the elasticity and tensile strength of skin. As wounds heal, collagen density, fiber size, and orientation all change to return the skin to a healthy state (*110*, *111*). The increased rate of wound closure, thicker epidermis, and increased collagen intensity seen in the Stim group highlight the device's ability to promote effective healing beyond simply accelerating wound closure.

Immunohistochemical staining results further support improvements in healing for wounds treated with WPED. Previous studies in human and animal models of wound healing show the ability of electrical stimulation to promote angiogenesis, which facilitates the transport of oxygen and nutrients to the wound site (*27*, *56*, *112*, *113*). CD31 (also known as PECAM-1) is a commonly used biomarker to identify blood vessels (*114*). CD31 staining is notably higher ($P < 0.05$) for the Stim group than for the Sham or Control groups (Fig. 6E). In addition, as a wound progresses through the phases of wound healing, from inflammation to proliferation and remodeling, pro-inflammatory M1 macrophages are replaced with M2 macrophages that promote cell proliferation and tissue remodeling (*115*, *116*). Figure 6F shows staining for F4/80 (a pan-macrophage marker) and inducible nitric oxide synthase (iNOS; an M1 marker) or CD206 (an M2 marker). A substantially ($P = 0.007$) lower ratio of M1 to M2 markers is seen in the Stim group compared to the Sham and Control groups (Fig. 6G), but no notable difference between the Sham and Control groups is observed. The low M1/M2 macrophage ratio suggests that WPED itself does not trigger an inflammatory response and that electrotherapy offered by WPED reduces inflammation, as previously reported for wounds treated with electrotherapy (*117*–*119*). Chronic wounds often fail to exit the inflammatory phase (*116*, *120*, *121*); as such, the anti-inflammatory characteristics of WPED further render it useful for chronic wound treatment.

Reported examples of electrical stimulation–based devices offer increases in CD31 staining (*27*, *29*, *49*), epidermal thickness (*25*, *49*), collagen intensity (*27*), and a shift in the ratio of M1 to M2 macrophages (*28*). Likewise, other wound-healing technologies show increased CD31 expression, epidermal thickness, and collagen expression (*56*, *122*, *123*). The user-friendly WPED offers similar pro-healing capabilities at a fraction of the cost compared to the above-referenced technologies, making it preferable for treating wounds.

DISCUSSION

This work describes a low-cost, electronics-free, water-powered dressing for delivering electrotherapy that accelerates wound healing at rates comparable to those offered by expensive therapeutics. The technology uses an Mg-Ag/AgCl battery with a cellulose separator. The addition of a small amount of water activates the battery, which provides on-demand electrical stimulation for several hours even when the system is subjected to extreme strains. Our benchtop studies further show that tailoring the battery size enables continuous electrical stimulation over several days thus circumventing the need for daily replacement of the dressing. This device is lightweight and highly flexible and can be easily integrated into existing bandages. The manufacturing versatility enables the realization of electrotherapy dressings with advanced 3D morphable kirigami electrodes that can be readily configured to treat wounds of different shapes, sizes, and contours. In addition, the device requires no external electronics or specialized knowledge, rendering it ideal for point-of-care treatment.

The device is validated in a diabetic mouse wound-healing model. Wounds receiving electrotherapy show faster wound closure, with 75% of the wounds achieving total wound closure by day 11, compared with 12.5% for wounds treated with sham devices and 0% in the case of wounds with only occlusive dressing. Electrotherapy-treated wounds exhibit improved epidermal thickness and angiogenesis and reduced inflammation as compared with untreated mice and mice wearing sham devices.

The low-cost, easy-to-use technology described here offers great potential to improve wound healing in a wide range of settings, extreme weather conditions, and use cases. To expand the impact of this work, future research will investigate the device's efficacy in a porcine model of full-thickness dermal wound healing which is characterized by deep wounds (~1 cm) and more closely resembles human skin remodeling and wound healing. Such studies could further elucidate the precise molecular mechanisms by which the WPED promotes healing and allow testing of its ability to treat deep wounds. This would help translate the device toward human use. Furthermore, the effect of the device should be characterized in more depth by using advanced molecular biology techniques, for instance, flow cytometry, transcriptomics, and proteomics. Additional research should focus on investigating the effect of stimulation time on healing, as this is an underexplored area. Since the device can be modified to provide different amounts of stimulation, this would further allow for custom treatments specific to individual wounds. Several prior studies show that electrical stimulation can disrupt biofilms and inhibit bacterial infection in wounds (*124*, *125*). Future work will explore this device's ability to prevent infection as well as promote healing, expanding the device's impact as a regenerative technology.

MATERIALS AND METHODS

Fabrication of WPED

Battery

Screen printing of carbon ink (E3178, Ercon, USA) on a 75-μm-thick sheet of polyimide (PI; Argon Inc., CA, USA), subsequent baking at 120°C for 20 min, and CO_2 laser (Fusion Edge, Epilog, USA) patterning (speed: 10%; power: 3%; frequency: 7%) formed the current collectors for the anode and cathode. Anode fabrication involved applying a thin layer of carbon ink onto the laser patterned PI/carbon-based anode current collector followed by attaching a 100-μm-thick magnesium (Alibaba) ring to it, and baking at 120°C for 10 min. The cathode fabrication process comprised screen-printing Ag/AgCl ink (E2414, Ercon, USA) onto the cathode current collector and baking at 80° and 120°C each for 20 min. A separator with NaCl salt loadings of 2.4 mg/cm^2 was fabricated as described in a previous study (*59*). Insertion of a separator between the anode and cathode and packaging of the battery assembly within a laser-patterned waterproof tape (Gorilla Glue Inc., OH) completed the battery fabrication process.

Stimulation electrodes

Fabrication began by laser patterning of PI sheet, followed by the application of carbon ink on both sides and subsequent baking at 120°C for 10 min. Next, encapsulation of interconnects with epoxy resin (Epoxy Marine, Loctite, Henkel Corp., OH) defined the active electrode areas and contact pads.

WPED assembly

The process began with punching two 1.5-mm-diameter holes in a commercial 4.5 cm × 4.5 cm bandage (Tegaderm, 3M, USA) which served as apertures for connecting stimulation electrodes with the battery. Next, mounting the battery on top (nonadhesive side) and the stimulation electrode pair on the bottom (adhesive side) of the commercial bandage followed by bonding the IE to the contact pad of the anode (Mg electrode) and OE to the contact pad of the cathode (Ag/AgCl electrode) using carbon ink completed the WPED assembly process.

Simulation and experimental characterization of the mechanical properties of WPED

Full 3D finite element analysis (FEA) was carried out to predict the mechanical response of serpentine (width: 0.3 mm; thickness: 0.1 mm) and kirigami (width: 0.3 mm; thickness: 0.1 mm) stimulation electrodes with corresponding structure layouts and material properties using the Structural Mechanics Module in a commercial software (COMSOL Multiphysics 6.0). A tetrahedral meshing with maximum and minimum mesh sizes of ~0.3 and ~0.01 μm was used. The Young's modulus and Poisson's ratio were set at 2.5 GPa and 0.34 for PI and 110 GPa and 0.34 for carbon film, respectively, per literature (*45*, *126*, *127*). The motion of the serpentine and kirigami electrodes was simulated by fixing their base with a fixed support and deformation was applied to the tip of the electrodes with a pivot joint. Next, the distribution of stress/strain of electrodes under different stretching lengths was studied.

A custom-designed mechanical stretching machine was used to test the biaxial stress response of the self-similar serpentine outer ring electrode under different strains. Similarly, the spiral-shaped IE was fixed to a substrate and subjected to uniaxial strains perpendicular to the plane of the OE. The displacement of both the electrodes was measured with a digital caliper and their electrical resistance as a function of strain was captured using a digital multimeter.

Electromagnetic simulation of WPED

FEA was conducted using commercial software (COMSOL Multiphysics 6.0) to determine the electric potential and electric field generated and distributed during the electrical stimulation around the electrodes and in the wound area. The skin was composed of tissue layers that include stratum corneum (thickness: 0.25 mm), epidermis (thickness: 0.75 mm), dermis (thickness: 1.5 mm), and subcutis (thickness: 2.5 mm). The electrical conductivities of these four tissues were assumed to be 2×10^{-6}, 0.026, 0.222, and 0.08 S/m, respectively, while the relative permittivities were assumed to be 5×10^2, 5×10^6, 5×10^9, and 5×10^7, respectively, per literature (*25*).

The electric field was described by

$$\nabla . D = \rho$$

$$E = -\nabla V$$

where D is the electric displacement field, ρ is the charge density, E is the electric field, and V is the electric potential of the electrode.

The geometries of planar electrodes and tissue layers were modeled using tetrahedral mesh elements and placed around the wound. Furthermore, to ensure high accuracy of computation, a convergence test of the mesh size was performed. The potential of the cathode (outer ring electrode) and anode (inner disk electrode) was set to be 1.6 and 0 V, respectively.

Electrochemical, electrical, and thermal characterizations

Open circuit potentiometry, chronopotentiometry, and impedance spectroscopy measurements were performed using a potentiostat (PalmSens4, PalmSens, NL). The discharge behavior of batteries with different electrolytes was investigated using a multichannel potentiostat (MultiPalmSens4, PalmSens, NL) with current densities of 1 mA/cm^2 until the voltage dropped to 0 V. Studies investigating the duration of stimulation as a function of wound resistance were obtained by interfacing the battery to different load resistance and capturing the battery voltage using a digital multimeter (BT-90EPC, BTMeter, USA). Electrochemical impedance spectroscopy measurements were performed for frequencies ranging from 0.1 Hz to 100 kHz with an amplitude of 10-mV and 0-V bias. Thermograms were captured by a commercial IR camera (CompactPRO Fastframe, Seek Thermal, USA). Humidity-controlled experiments were conducted in a testing chamber that consisted of a humidity generator (HUL535W, Honeywell, USA), a dehumidifier (TP30WKN, Honeywell, USA), and a humidity controller (IHC-200, INKBIRD, CN). All tests were carried out at room temperature unless otherwise stated. All experiments were repeated four times ($n = 4$) and data were reported as average ± SD.

In vitro biocompatibility test

In vitro biocompatibility testing was performed by using media that had been incubated with the device for cell culture. To prepare the incubated media, one device was incubated in 3 ml of Dulbecco's modified Eagle's medium (DMEM) with 10% fetal bovine serum (FBS) for at least 24 hours. DMEM with 10% FBS was used as control media. Wild-type mouse embryonic fibroblasts (NIH/3T3, ATCC CRL-1658, American Type Culture Collection) were plated in a 24-well plate ($N = 3$ per group). All cells were plated at a density of 10,000 and were incubated for 24 hours in control media. After 24 hours, treated cells were switched to incubated media. This was denoted as time $t = 0$. At 24 and 48 hours after $t = 0$, the media were aspirated, the cells were rinsed with phosphate-buffered saline, and fresh media (either incubated or control) were applied. At 72 hours, a live/dead staining kit (L3224, Invitrogen) was performed according to the manufacturer's protocol. The cells were imaged using a fluorescence microscope (DMI6000 B, Leica). The cell viability was quantified using ImageJ (NIH, 1.53s).

In vitro scratch assay

Mouse NIH/3T3 fibroblasts were cultured in DMEM with 10% FBS for use in the in vitro cell migration assay. Stimulation electrodes were fabricated on the bottom of 50-mm petri dishes and were connected to WPED via wires. Such a setup enabled a flat surface for culturing cells while also avoiding direct contact of the battery with the culture media. A total of 5×10^5 fibroblasts were plated on each dish and were grown to confluence. Scratches were made between the anode and cathode of the electrode using a 200-μl pipette tip

and the media were changed to DMEM with 5% FBS. Electrical stimulation was applied to the cells by connecting the electrodes to WPED. The cells were imaged after 24 hours and quantitative analysis was performed using ImageJ.

In vivo diabetic mouse wound-healing model

All animal procedures were approved by Columbia University Animal Care and Use Committee (protocol AC-AABK5600) and were carried out in accordance with the approved guidelines. Male diabetic (db/db) mice (strain no. 000697, The Jackson Laboratory) were obtained and acclimated to the facility for at least 4 days before surgery. Before surgery, mice had their blood glucose measured with a commercially available glucometer (Contour, Bayer) to ensure that their blood levels were >250 mg dl^{-1}. For surgery, mice (ages 11 to 13 weeks) were anesthetized using isoflurane. The fur was removed from the dorsum by shaving and using a depilatory cream and a full-thickness dorsal wound was made using a 10-mm biopsy punch. The stimulating devices were activated using a small volume of water and the voltage across the device was verified to be between 1.5 and 1.7 V using a multimeter (U1272A, Keysight Technologies). The stimulating devices or sham devices were immediately placed on the wound and adhered to the skin with an occlusive dressing (Tegaderm, 3M). Control mice received occlusive dressing only. The mice were housed individually after surgery. On subsequent days, the mice were anesthetized using isoflurane, and the dressings and devices were removed. The wounds were photographed with a standard iPhone SE camera. Wound closure was quantified using ImageJ, where open wound was considered areas where moist tissue was visible (*39*, *128*). Wounds were considered completely closed when there was no drainage and no moist tissue visible, and the wounds were completely re-epithelialized. Fresh devices were applied daily to the wounds and affixed with occlusive dressing.

Histology and staining

Wound tissue was collected from euthanized mice 13 days after the surgery was performed. The tissue was fixed in 4% formaldehyde for over 24 hours. The Columbia University Molecular Pathology Shared Resource (MPSR) facility embedded the tissue in paraffin, sectioned the tissue into slices of 5 μm, and performed H&E and MTS. Whole-slide scanning of the H&E and MST slides was performed by the MPSR facility using an Aperio AT2 scanner (Leica) at 40×.

For immunofluorescence staining, slides were deparaffinized in xylene and rehydrated in a descending ethanol rehydration series. When staining for CD31, citrate buffer heat–induced antigen retrieval was used. When staining for F4/80 with iNOS or CD206, trypsin-based antigen retrieval was used. Slides were blocked for 2 hours in serum solution (1% bovine serum albumin) and were incubated with primary antibody at 4°C overnight. The primary antibodies used were rabbit recombinant anti-CD31 (1:200; Abcam, ab281583), rat monoclonal anti-F4/80 (1:100; eBioscience, 53-4801-82), rabbit polyclonal anti-iNOS (1:100; Abcam, ab3523), and rabbit polyclonal anti-mannose receptor (1:200; Abcam, ab64693). The secondary antibody used was goat anti-rabbit IgG (H + L) Secondary Antibody, Alexa Fluor 594 (1:500; Invitrogen A11037). Antifade mounting medium with 4′,6-diamidino-2-phenylindole (DAPI) for nuclear counterstaining was used (ProLong Gold Antifade Mountant with DAPI, Invitrogen). Images were obtained at ×10 magnification using a Nikon Ti Eclipse inverted microscope.

Tissue analysis

Aperio ImageScope (Leica Biosystems, v12.4.3) was used to quantify epidermal thickness from H&E images. Three epidermal measurements from across the wound were taken per image. For each MTS, three square images of the collagen from across the wound were extracted at 40×, and ImageJ was used to quantify the intensity. Immunofluorescence staining for CD31 was quantified as fluorescence intensity for areas of the same size taken across the wound. For macrophage analysis, M1 macrophages were counted as structures that stained positively for both F4/80 and iNOS; M2 macrophages were counted as structures that stained positively for both F4/80 and CD206.

Movement analysis

Mice wearing either stimulating devices, sham devices, or Tegaderm only were individually placed in a 28 cm × 17 cm standard cage and were allowed to freely explore. Mice were recorded for 10 min from a standardized distance above the cage. DeepLabCut (version 2.3.7) (*129*, *130*) was used to analyze the videos. A total of 250 frames taken from 12 videos were analyzed using a ResNet-50–based with default parameters for 10,000 training iterations. The test error was 2.31 pixels, and the train error was 2.46 pixels (image size was 1920 pixels by 1080 pixels). We then used a p-cutoff of 0.7 to condition the *X*, *Y* coordinates for future analysis. This network was then used to analyze videos from similar experimental settings.

Supplementary Materials

This PDF file includes:

Supplementary Text
Figs. S1 to S14
Tables S1 to S4
Legends for movies S1 to S3
References

Other Supplementary Material for this manuscript includes the following:

Movies S1 to S3

REFERENCES AND NOTES

1. L. Martinengo, M. Olsson, R. Bajpai, M. Soljak, Z. Upton, A. Schmidtchen, J. Car, K. Järbrink, Prevalence of chronic wounds in the general population: Systematic review and meta-analysis of observational studies. *Ann. Epidemiol.* **29**, 8–15 (2019).
2. L. M. Morton, T. J. Phillips, Wound healing and treating wounds: Differential diagnosis and evaluation of chronic wounds. *J. Am. Acad. Dermatol.* **74**, 589–605 (2016).
3. V. Falanga, R. R. Isseroff, A. M. Soulika, M. Romanelli, D. Margolis, S. Kapp, M. Granick, K. Harding, Chronic wounds. *Nat. Rev. Prim.* **8**, 50 (2022).
4. S. R. Nussbaum, M. J. Carter, C. E. Fife, J. DaVanzo, R. Haught, M. Nusgart, D. Cartwright, An economic evaluation of the impact, cost, and medicare policy implications of chronic nonhealing wounds. *Value Health* **21**, 27–32 (2018).
5. X. Zhu, M. M. Olsson, R. Bajpai, K. Järbrink, W. E. Tang, J. Car, Health-related quality of life and chronic wound characteristics among patients with chronic wounds treated in primary care: A cross-sectional study in Singapore. *Int. Wound J.* **19**, 1121–1132 (2022).
6. J. G. Powers, C. Higham, K. Broussard, T. J. Phillips, Wound healing and treating wounds: Chronic wound care and management. *J. Am. Acad. Dermatol.* **74**, 607–625 (2016).
7. G. A. Kannon, A. B. Garrett, Moist wound healing with occlusive dressings: A clinical review. *Dermatol. Surg.* **21**, 583–590 (1995).
8. Y. Liang, J. He, B. Guo, Functional hydrogels as wound dressing to enhance wound healing. *ACS Nano* **15**, 12687–12722 (2021).
9. C. Bay, Z. Chizmar, E. M. Reece, J. Z. Yu, J. Winocour, J. Vorstenbosch, S. Winocour, Comparison of skin substitutes for acute and chronic wound management. *Semin. Plast. Surg.* **35**, 171–180 (2021).
10. T. J. Wieman, J. M. Smiell, Y. Su, Efficacy and safety of a topical gel formulation of recombinant human platelet-derived growth factor-BB (becaplermin) in patients with chronic neuropathic diabetic ulcers. A phase III randomized placebo-controlled double-blind study. *Diabetes Care* **21**, 822–827 (1998).
11. F. Tecilazich, T. Dinh, A. Veves, Treating diabetic ulcers. *Expert Opin. Pharmacother.* **12**, 593–606 (2011).

12. C. M. Zelen, T. E. Serena, L. Gould, L. Le, M. J. Carter, J. Keller, W. W. Li, Treatment of chronic diabetic lower extremity ulcers with advanced therapies: A prospective, randomised, controlled, multi-centre comparative study examining clinical efficacy and cost. *Int. Wound J.* **13**, 272–282 (2016).
13. Q. Yu, H. Sun, Z. Yue, C. Yu, L. Jiang, X. Dong, M. Yao, M. Shi, L. Liang, Y. Wan, H. Zhang, F. Yao, J. Li, Zwitterionic polysaccharide-based hydrogel dressing as a stem cell carrier to accelerate burn wound healing. *Adv. Heal. Mater.* **12**, e2202309 (2023).
14. S. Chen, H. Wang, Y. Su, J. V. John, A. McCarthy, S. L. Wong, J. Xie, Mesenchymal stem cell-laden, personalized 3D scaffolds with controlled structure and fiber alignment promote diabetic wound healing. *Acta Biomater.* **108**, 153–167 (2020).
15. L. C. Hsu, B. Y. Peng, M. S. Chen, B. Thalib, M. Ruslin, T. D. X. Tung, H. H. Chou, K. L. Ou, The potential of the stem cells composite hydrogel wound dressings for promoting wound healing and skin regeneration: In vitro and in vivo evaluation. *J. Biomed. Mater. Res. B Appl. Biomater.* **107**, 278–285 (2019).
16. X. Dong, X. Lu, K. Kingston, E. Brewer, B. A. Juliar, O. D. Kripfgans, J. B. Fowlkes, R. T. Franceschi, A. J. Putnam, Z. Liu, M. L. Fabiilli, Controlled delivery of basic fibroblast growth factor (bFGF) using acoustic droplet vaporization stimulates endothelial network formation. *Acta Biomater.* **97**, 409–419 (2019).
17. J. Chi, X. Zhang, C. Chen, C. Shao, Y. Zhao, Y. Wang, Antibacterial and angiogenic chitosan microneedle array patch for promoting wound healing. *Bioact. Mater.* **5**, 253–259 (2020).
18. A. Vijayan, A. Sabareeswaran, G. S. V. Kumar, PEG grafted chitosan scaffold for dual growth factor delivery for enhanced wound healing. *Sci. Rep.* **9**, 19165 (2019).
19. K. Nuutila, M. Samandari, Y. Endo, Y. Zhang, J. Quint, T. A. Schmidt, A. Tamayol, I. Sinha, In vivo printing of growth factor-eluting adhesive scaffolds improves wound healing. *Bioact. Mater.* **8**, 296–308 (2021).
20. Y. Xiong, L. Chen, P. Liu, T. Yu, C. Lin, C. Yan, Y. Hu, W. Zhou, Y. Sun, A. C. Panayi, F. Cao, H. Xue, L. Hu, Z. Lin, X. Xie, X. Xiao, Q. Feng, B. Mi, G. Liu, All-in-one: Multifunctional hydrogel accelerates oxidative diabetic wound healing through timed-release of exosome and fibroblast growth factor. *Small* **18**, e2104229 (2022).
21. A. Joshi, Z. Xu, Y. Ikegami, K. Yoshida, Y. Sakai, A. Joshi, T. Kaur, Y. Nakao, Y. Yamashita, H. Baba, S. Aishima, N. Singh, H. Ijima, Exploiting synergistic effect of externally loaded bFGF and endogenous growth factors for accelerated wound healing using heparin functionalized PCL/gelatin co-spun nanofibrous patches. *Chem. Eng. J.* **404**, 126518 (2021).
22. S. Haldar, A. Sharma, S. Gupta, S. Chauhan, P. Roy, D. Lahiri, Bioengineered smart trilayer skin tissue substitute for efficient deep wound healing. *Mater. Sci. Eng. C* **105**, 110140 (2019).
23. S. Vakilian, F. Jamshidi-adegani, A. A. Yahmadi, M. Al-Broumi, N. U. Rehman, M. U. Anwar, K. Alam, N. Al-Wahaibi, A. Shalaby, S. Alyaqoobi, A. Al-Harrasi, K. Mustafa, S. Al-Hashmi, A competitive nature-derived multilayered scaffold based on chitosan and alginate, for full-thickness wound healing. *Carbohydr. Polym.* **262**, 117921 (2021).
24. M. I. E. Molina, K. G. Malollari, K. Komvopoulos, Design challenges in polymeric scaffolds for tissue engineering. *Front. Bioeng. Biotechnol.* **9**, 617141 (2021).
25. J. W. Song, H. Ryu, W. Bai, Z. Xie, A. Vázquez-Guardado, K. Nandoliya, R. Avila, G. Lee, Z. Song, J. Kim, M.-K. Lee, Y. Liu, M. Kim, H. Wang, Y. Wu, H.-J. Yoon, S. S. Kwak, J. Shin, K. Kwon, W. Lu, X. Chen, Y. Huang, G. A. Ameer, J. A. Rogers, Bioresorbable, wireless, and battery-free system for electrotherapy and impedance sensing at wound sites. *Sci. Adv.* **9**, eade4687 (2023).
26. E. S. Sani, C. Xu, C. Wang, Y. Song, J. Min, J. Tu, S. A. Solomon, J. Li, J. L. Banks, D. G. Armstrong, W. Gao, A stretchable wireless wearable bioelectronic system for multiplexed monitoring and combination treatment of infected chronic wounds. *Sci. Adv.* **9**, eadf7388 (2023).
27. Y. Jiang, A. A. Trotsyuk, S. Niu, D. Henn, K. Chen, C.-C. Shih, M. R. Larson, A. M. Mermin-Bunnell, S. Mittal, J.-C. Lai, A. Saberi, E. Beard, S. Jing, D. Zhong, S. R. Steele, K. Sun, T. Jain, E. Zhao, C. R. Neimeth, W. G. Viana, J. Tang, D. Sivaraj, J. Padmanabhan, M. Rodrigues, D. P. Perrault, A. Chattopadhyay, Z. N. Maan, M. C. Leeolou, C. A. Bonham, S. H. Kwon, H. C. Kussie, K. S. Fischer, G. Gurusankar, K. Liang, K. Zhang, R. Nag, M. P. Snyder, M. Januszyk, G. C. Gurtner, Z. Bao, Wireless, closed-loop, smart bandage with integrated sensors and stimulators for advanced wound care and accelerated healing. *Nat. Biotechnol.* **41**, 652–662 (2023).
28. S. M. Yang, H. Kim, G.-J. Ko, J. C. Choe, J. H. Lee, K. Rajaram, B. An, W. B. Han, D.-J. Kim, J.-W. Shin, T.-M. Jang, H. Kang, S. Han, K. Lee, S. J. Oh, S.-W. Hwang, Soft, wireless electronic dressing system for wound analysis and biophysical therapy. *Nano Today* **47**, 101685 (2022).
29. C. Wang, X. Jiang, H. J. Kim, S. Zhang, X. Zhou, Y. Chen, H. Ling, Y. Xue, Z. Chen, M. Qu, L. Ren, J. Zhu, A. Libanori, Y. Zhu, H. Kang, S. Ahadian, M. R. Dokmeci, P. Servati, X. He, Z. Gu, W. Sun, A. Khademhosseini, Flexible patch with printable and antibacterial conductive hydrogel electrodes for accelerated wound healing. *Biomaterials* **285**, 121479 (2022).
30. F. Ershad, A. Thukral, J. Yue, P. Comeaux, Y. Lu, H. Shim, K. Sim, N.-I. Kim, Z. Rao, R. Guevara, L. Contreras, F. Pan, Y. Zhang, Y.-S. Guan, P. Yang, X. Wang, P. Wang, X. Wu, C. Yu, Ultra-conformal drawn-on-skin electronics for multifunctional motion artifact-free sensing and point-of-care treatment. *Nat. Commun.* **11**, 3823 (2020).
31. C. Chen, X. Bai, Y. Ding, I. S. Lee, Electrical stimulation as a novel tool for regulating cell behavior in tissue engineering. *Biomater. Res.* **23**, 25 (2019).
32. G. Thakral, J. LaFontaine, B. Najafi, T. K. Talal, P. Kim, L. A. Lavery, Electrical stimulation to accelerate wound healing. *Diabet. Foot Ankle* **4**, 10.3402/dfa.v4i0.22081 (2013).
33. R. Luo, J. Dai, J. Zhang, Z. Li, Accelerated skin wound healing by electrical stimulation. *Adv. Heal. Mater.* **10**, 2100557 (2021).
34. P. E. Houghton, Electrical stimulation therapy to promote healing of chronic wounds: A review of reviews. *Chronic Wound Care Manag. Res.* **4**, 25–44 (2017).
35. J. M. Wood, P. E. Evans, K. U. Schallreuter, W. E. Jacobson, R. Sufit, J. Newman, C. White, M. Jacobson, A multicenter study on the use of pulsed low-intensity direct current for healing chronic stage II and stage III decubitus ulcers. *Arch. Dermatol.* **129**, 999–1009 (1993).
36. P. E. Houghton, C. B. Kincaid, M. Lovell, K. E. Campbell, D. H. Keast, M. G. Woodbury, K. A. Harris, Effect of electrical stimulation on chronic leg ulcer size and appearance. *Res. Rep. Phys. Ther.* **83**, 17–29 (2003).
37. A. Janković, I. Binić, Frequency rhythmic electrical modulation system in the treatment of chronic painful leg ulcers. *Arch. Dermatol. Res.* **300**, 377–383 (2008).
38. G. Xu, Y. Lu, C. Cheng, X. Li, J. Xu, Z. Liu, J. Liu, G. Liu, Z. Shi, Z. Chen, F. Zhang, Y. Jia, D. Xu, W. Yuan, Z. Cui, S. S. Low, Q. Liu, Battery-free and wireless smart wound dressing for wound infection monitoring and electrically controlled on-demand drug delivery. *Adv. Funct. Mater.* **31**, 1–14 (2021).
39. Y. Long, H. Wei, J. Li, G. Yao, B. Yu, D. Ni, A. L. Gibson, X. Lan, Y. Jiang, W. Cai, X. Wang, Effective wound healing enabled by discrete alternative electric fields from wearable nanogenerators. *ACS Nano* **12**, 12533–12540 (2018).
40. S. Du, H. Suo, G. Xie, Q. Lyu, M. Mo, Z. Xie, N. Zhou, L. Zhang, J. Tao, J. Zhu, Self-powered and photothermal electronic skin patches for accelerating wound healing. *Nano Energy* **93**, 106906 (2022).
41. S. Du, N. Zhou, G. Xie, Y. Chen, H. Suo, J. Xu, J. Tao, L. Zhang, J. Zhu, Surface-engineered triboelectric nanogenerator patches with drug loading and electrical stimulation capabilities: Toward promoting infected wounds healing. *Nano Energy* **85**, 106004 (2021).
42. H. Kai, T. Yamauchi, Y. Ogawa, A. Tsubota, T. Magome, T. Miyake, K. Yamasaki, M. Nishizawa, Accelerated wound healing on skin by electrical stimulation with a bioelectric plaster. *Adv. Heal. Mater.* **6**, 1700465 (2017).
43. D. S. Howe, J. L. Dunning, M. K. Henzel, J. K. Graebert, K. M. Bogie, A wearable stimulation bandage for electrotherapy studies in a rat ischemic wound model. *Proc. Annu. Int. Conf. IEEE Eng. Med. Biol. Soc. EMBS* **2011**, 298–301 (2011).
44. R. Kaveti, J. Kim, Flexible wireless power transfer module implemented with aerojet-printing and laser-sintering of rigid NiZn-ferrite ceramic films. *Nano Energy* **57**, 317–326 (2019).
45. J. Park, K. Kim, Y. Kim, T. S. Kim, I. S. Min, B. Li, Y. U. Cho, C. Lee, J. Y. Lee, Y. Gao, K. Kang, D. H. Kim, W. J. Choi, H. B. Shin, H. K. Kang, Y. M. Song, H. Cheng, I. J. Cho, K. J. Yu, A wireless, solar-powered, optoelectronic system for spatial restriction-free long-term optogenetic neuromodulations. *Sci. Adv.* **9**, eadi8918 (2023).
46. T. V. Boyko, M. T. Longaker, G. P. Yang, Review of the current management of pressure ulcers. *Adv. Wound Care* **7**, 57–67 (2018).
47. G. Yao, D. Jiang, J. Li, L. Kang, S. Chen, Y. Long, Y. Wang, P. Huang, Y. Lin, W. Cai, X. Wang, Self-activated electrical stimulation for effective hair regeneration via a wearable omnidirectional pulse generator. *ACS Nano* **13**, 12345–12356 (2019).
48. R. Luo, Y. Liang, J. Yang, H. Feng, Y. Chen, X. Jiang, Z. Zhang, J. Liu, Y. Bai, J. Xue, S. Chao, Y. Xi, X. Liu, E. Wang, D. Luo, Z. Li, J. Zhang, Reshaping the endogenous electric field to boost wound repair via electrogenerative dressing. *Adv. Mater.* **35**, e2208395 (2023).
49. S. R. Barman, S.-W. Chan, F.-C. Kao, H.-Y. Ho, I. Khan, A. Pal, C.-C. Huang, Z.-H. Lin, A self-powered multifunctional dressing for active infection prevention and accelerated wound healing. *Sci. Adv.* **9**, eadc8758 (2023).
50. T. Li, C. Shi, F. Jin, F. Yang, L. Gu, T. Wang, W. Dong, Z.-Q. Feng, Cell activity modulation and its specific function maintenance by bioinspired electromechanical nanogenerator. *Sci. Adv.* **9**, eabh2350 (2021).
51. R. Mao, B. Yu, J. Cui, Z. Wang, X. Huang, H. Yu, K. Lin, S. G. F. Shen, Piezoelectric stimulation from electrospun composite nanofibers for rapid peripheral nerve regeneration. *Nano Energy* **98**, 107322 (2022).
52. B. Yu, Z. Qiao, J. Cui, M. Lian, Y. Han, X. Zhang, W. Wang, X. Yu, H. Yu, X. Wang, K. Lin, A host-coupling bio-nanogenerator for electrically stimulated osteogenesis. *Biomaterials* **276**, 120997 (2021).
53. G. Yao, L. Kang, C. Li, S. Chen, Q. Wang, J. Yang, Y. Long, J. Li, K. Zhao, W. Xu, W. Cai, Y. Lin, X. Wang, A self-powered implantable and bioresorbable electrostimulation device for biofeedback bone fracture healing. *Proc. Natl. Acad. Sci. U A* **118**, e2100772118 (2021).
54. E. K. LeGrand, Preclinical promise of becaplermin (rhPDGF-BB) in wound healing. *Am. J. Surg.* **176**, 48S–54S (1998).
55. T. T. Nguyen, D. Ding, W. R. Wolter, R. L. Pérezpérez, M. M. Champion, K. V. Mahasenan, D. Hesek, M. Lee, V. A. Schroeder, J. I. Jones, E. Lastochkin, M. K. Rose, C. E. Peterson, M. A. Suckow, S. Mobashery, M. Chang, Validation of matrix metalloproteinase-9 (MMP-9) as a novel target for treatment of diabetic foot ulcers in humans and discovery of a

potent and selective small-molecule MMP-9 inhibitor that accelerates healing. *J. Med. Chem.* **61**, 8825–8837 (2018).
56. G. Theocharidis, H. Yuk, H. Roh, L. Wang, I. Mezghani, J. Wu, A. Kafanas, M. Contreras, B. Sumpio, Z. Li, E. Wang, L. Chen, C. F. Guo, N. Jayaswal, X. L. Katopodi, N. Kalavros, C. S. Nabzdyk, I. S. Vlachos, A. Veves, X. Zhao, A strain-programmed patch for the healing of diabetic wounds. *Nat. Biomed. Eng.* **6**, 1118–1133 (2022).
57. G. Li, C.-N. Ko, D. Li, C. Yang, W. Wang, G.-J. Yang, C. Primo, V. K. W. Wong, Y. Xiang, L. Lin, D.-L. Ma, C.-H. Leung, A small molecule HIF-1α stabilizer that accelerates diabetic wound healing. *Nat. Commun.* **12**, 3363 (2021).
58. W. Srifa, N. Kosaric, A. Amorin, O. Jadi, Y. Park, S. Mantri, J. Camarena, G. C. Gurtner, M. Porteus, Cas9-AAV6-engineered human mesenchymal stromal cells improved cutaneous wound healing in diabetic mice. *Nat. Commun.* **11**, 2470 (2020).
59. A. J. Bandodkar, S. P. Lee, I. Huang, W. Li, S. Wang, C. J. Su, W. J. Jeang, T. Hang, S. Mehta, N. Nyberg, P. Gutruf, J. Choi, J. Koo, J. T. Reeder, R. Tseng, R. Ghaffari, J. A. Rogers, Sweat-activated biocompatible batteries for epidermal electronic and microfluidic systems. *Nat. Electron.* **3**, 554–562 (2020).
60. N. Mishra, N. T. Garland, K. A. Hewett, M. Shamsi, M. D. Dickey, A. J. Bandodkar, A soft wearable microfluidic patch with finger-actuated pumps and valves for on-demand, longitudinal, and multianalyte sweat sensing. *ACS Sens.* **7**, 3169–3180 (2022).
61. L. Yin, M. Cao, K. N. Kim, M. Lin, J.-M. Moon, J. R. Sempionatto, J. Yu, R. Liu, C. Wicker, A. Trifonov, F. Zhang, H. Hu, J. R. Moreto, J. Go, S. Xu, J. Wang, A stretchable epidermal sweat sensing platform with an integrated printed battery and electrochromic display. *Nat. Electron.* **5**, 694–705 (2022).
62. M. Szycher, S. J. Lee, Modern wound dressings: A systematic approach to wound healing. *J. Biomater. Appl.* **7**, 142–213 (1992).
63. A. K. Brooks, S. Chakravarty, M. Ali, V. K. Yadavalli, Kirigami-inspired biodesign for applications in healthcare. *Adv. Mater.* **34**, e2109550 (2022).
64. Y. Morikawa, S. Yamagiwa, H. Sawahata, R. Numano, K. Koida, T. Kawano, Donut-shaped stretchable kirigami: Enabling electronics to integrate with the deformable muscle. *Adv. Heal. Mater.* **8**, e1900939 (2019).
65. R. Rahimi, M. Ochoa, A. Tamayol, S. Khalili, A. Khademhosseini, B. Ziaie, Highly stretchable potentiometric pH sensor fabricated via laser carbonization and machining of carbon−polyaniline composite. *ACS Appl. Mater. Interfaces* **9**, 9015–9023 (2017).
66. M. Galliani, C. Diacci, M. Berto, M. Sensi, V. Beni, M. Berggren, M. Borsari, D. T. Simon, F. Biscarini, C. A. Bortolotti, Flexible printed organic electrochemical transistors for the detection of uric acid in artificial wound exudate. *Adv. Mater. Interfaces* **7**, 1–7 (2020).
67. N. T. Garland, J. W. Song, T. Ma, Y. J. Kim, A. Vázquez-Guardado, A. B. Hashkavayi, S. K. Ganeshan, N. Sharma, H. Ryu, M. K. Lee, B. Sumpio, M. A. Jakus, V. Forsberg, R. Kaveti, S. K. Sia, A. Veves, J. A. Rogers, G. A. Ameer, A. J. Bandodkar, A. Miniaturized, Battery-free, wireless wound monitor that predicts wound closure rate early. *Adv. Heal. Mater.* **12**, e2301280 (2023).
68. X. Pei, H. Jin, S. Dong, D. Lou, L. Ma, X. Wang, W. Cheng, H. Wong, Flexible wireless skin impedance sensing system for wound healing assessment. *Vacuum* **168**, 108808 (2019).
69. M. Zhao, B. Song, J. Pu, T. Wada, B. Reid, G. Tai, F. Wang, A. Guo, P. Walczysko, Y. Gu, T. Sasaki, A. Suzuki, J. V. Forrester, H. R. Bourne, P. N. Devreotes, C. D. Mccaig, J. M. Penninger, Electrical signals control wound healing through phosphatidylinositol-3-OH kinase-γ and PTEN. *Nature* **442**, 457–460 (2006).
70. T. B. Saw, X. Gao, M. Li, J. He, A. P. Le, S. Marsh, K. Lin, A. Ludwig, J. Prost, C. T. Lim, Transepithelial potential difference governs epithelial homeostasis by electromechanics. *Nat. Phys.* **18**, 1122–1128 (2022).
71. J. S. Petrofsky, D. Lawson, L. Berk, H. Suh, Enhanced healing of diabetic foot ulcers using local heat and electrical stimulation for 30 min three times per week. *J. Diabetes* **2**, 41–46 (2010).
72. J. A. Feedar, L. C. Kloth, G. D. Gentzkow, Chronic dermal ulcer healing enhanced with monophasic pulsed electrical stimulation. *Phys. Ther. Rehabil. J.* **71**, 639–649 (1991).
73. Y. Guo, W. Guan, C. Lei, H. Lu, W. Shi, G. Yu, Scalable super hygroscopic polymer films for sustainable moisture harvesting in arid environments. *Nat. Commun.* **13**, 2761 (2022).
74. F. Deng, Z. Chen, C. Wang, C. Xiang, P. Poredoš, R. Wang, Hygroscopic porous polymer for sorption-based atmospheric water harvesting. *Adv. Sci.* **9**, e2204724 (2022).
75. L. Wei, Z. Gao, Recent research advances on corrosion mechanism and protection, and novel coating materials of magnesium alloys: A review. *RSC Adv.* **13**, 8427–8463 (2023).
76. J. Gao, X. Li, Q. Liu, H. Fan, S. Gao, Y. Song, E. Wang, A chloride-free electrolyte to suppress the anodic hydrogen evolution corrosion of magnesium anode in aqueous magnesium air batteries. *Chem. Eng. J.* **464**, 142655 (2023).
77. S. Bhattacharya, R. Mishra, Pressure ulcers: Current understanding and newer modalities of treatment. *Indian J. Plast. Surg.* **48**, 4–16 (2015).
78. J. W. Kwak, M. Han, Z. Xie, H. U. Chung, J. Y. Lee, R. Avila, J. Yohay, X. Chen, C. Liang, M. Patel, I. Jung, J. Kim, M. Namkoong, K. Kwon, X. Guo, C. Ogle, D. Grande, D. Ryu, D. H. Kim, S. Madhvapathy, C. Liu, D. S. Yang, Y. Park, R. Caldwell, A. Banks, S. Xu, Y. Huang, S. Fatone, J. A. Rogers, Wireless sensors for continuous, multimodal measurements at the skin interface with lower limb prostheses. *Sci. Transl. Med.* **12**, eabc4327 (2020).
79. S. Han, J. Kim, S. M. Won, Y. Ma, D. Kang, Z. Xie, K. T. Lee, H. U. Chung, A. Banks, S. Min, S. Y. Heo, C. R. Davies, J. W. Lee, C. H. Lee, B. H. Kim, K. Li, Y. Zhou, C. Wei, X. Feng, Y. Huang, J. A. Rogers, Battery-free, wireless sensors for full-body pressure and temperature mapping. *Sci. Transl. Med.* **10**, eaan4950 (2018).
80. B. Reid, M. Zhao, The electrical response to injury: Molecular mechanisms and wound healing. *Adv. Wound Care* **3**, 184–201 (2014).
81. D. J. Cohen, W. J. Nelson, M. M. Maharbiz, Galvanotactic control of collective cell migration in epithelial monolayers. *Nat. Mater.* **13**, 409–417 (2014).
82. B. Song, Y. Gu, J. Pu, B. Reid, Z. Zhao, M. Zhao, Application of direct current electric fields to cells and tissues in vitro and modulation of wound electric field in vivo. *Nat. Protoc.* **2**, 1479–1489 (2007).
83. A. A. Al-Majed, T. M. Brushart, T. Gordon, Electrical stimulation accelerates and increases expression of BDNF and trkB mRNA in regenerating rat femoral motoneurons. *Eur. J. Neurosci.* **12**, 4381–4390 (2000).
84. A. A. Al-Majed, L. T. Siu, T. Gordon, Electrical stimulation accelerates and enhances expression of regeneration-associated genes in regenerating rat femoral motoneurons. *Cell. Mol. Neurobiol.* **24**, 379–402 (2004).
85. A. N. Koppes, A. M. Seggio, D. M. Thompson, Neurite outgrowth is significantly increased by the simultaneous presentation of Schwann cells and moderate exogenous electric fields. *J. Neural Eng.* **8**, 046023 (2011).
86. W. Jing, Y. Zhang, Q. Cai, G. Chen, L. Wang, X. Yang, W. Zhong, Study of electrical stimulation with different electric-field intensities in the regulation of the differentiation of PC12 cells. *ACS Chem. Nerosci.* **10**, 348–357 (2019).
87. A. N. Koppes, A. L. Nordberg, G. M. Paolillo, N. M. Goodsell, H. A. Darwish, L. Zhang, D. M. Thompson, Electrical stimulation of schwann cells promotes sustained increases in neurite outgrowth. *Tissue Eng. - Part A* **20**, 494–506 (2014).
88. S. Ud-Din, A. Bayat, Electrical stimulation and cutaneous wound healing: A review of clinical evidence. *Healthcare* **2**, 445–467 (2014).
89. X. Li, J. Kolega, Effects of direct current electric fields on cell migration and actin filament distribution in bovine vascular endothelial cells. *J. Vasc. Res.* **39**, 391–404 (2002).
90. K. Katoh, Effects of electrical stimulation on the signal transduction-related proteins, c-Src and focal adhesion kinase, in fibroblasts. *Life* **12**, 531 (2022).
91. D.-H. Kim, D. Wirtz, Focal adhesion size uniquely predicts cell migration. *FASEB J.* **27**, 1351–1361 (2013).
92. S. Zhao, A. S. Mehta, M. Zhao, Biomedical applications of electrical stimulation. *Cell. Mol. Life Sci.* **77**, 2681–2699 (2020).
93. K. Katoh, Effects of electrical stimulation of the cell: Wound healing, cell proliferation, apoptosis, and signal transduction. *Med. Sci.* **11**, 11 (2023).
94. H. Bai, J. V. Forrester, M. Zhao, DC electric stimulation upregulates angiogenic factors in endothelial cells through activation of VEGF receptors. *Cytokine* **55**, 110–115 (2011).
95. G. Theocharidis, B. E. Thomas, D. Sarkar, H. L. Mumme, W. J. R. Pilcher, B. Dwivedi, T. Sandoval-Schaefer, R. F. Sîrbulescu, A. Kafanas, I. Mezghani, P. Wang, A. Lobao, I. S. Vlachos, B. Dash, H. C. Hsia, V. Horsley, S. S. Bhasin, A. Veves, M. Bhasin, Single cell transcriptomic landscape of diabetic foot ulcers. *Nat. Commun.* **13**, 181 (2022).
96. X. T. Wang, C. C. McKeever, P. Vonu, C. Patterson, P. Y. Liu, Dynamic histological events and molecular changes in excisional wound healing of diabetic db/db mice. *J. Surg. Res.* **238**, 186–197 (2019).
97. D. G. Greenhalgh, K. H. Sprugel, M. J. Murray, R. Rosst, PDGF and FGF stimulate wound healing in the genetically diabetic mouse. *Am. J. Pathol.* **136**, 1235–1246 (1990).
98. D. Philp, M. Badamchian, B. Scheremeta, M. Nguyen, A. L. Goldstein, H. K. Kleinman, Thymosin β4 and a synthetic peptide containing its actin-binding domain promote dermal wound repair in db/db diabetic mice and in aged mice. *Wound Repair Regen.* **11**, 19–24 (2003).
99. S. R. Sullivan, R. A. Underwood, N. S. Gibran, R. O. Sigle, M. L. Usui, W. G. Carter, J. E. Olerud, Validation of a model for the study of multiple wounds in the diabetic mouse (db/db). *Plast. Reconstr. Surg.* **113**, 953–960 (2004).
100. G. Zhao, P. C. Hochwalt, M. L. Usui, R. A. Underwood, P. K. Singh, G. A. James, P. S. Stewart, P. Fleckman, J. E. Olerud, Delayed wound healing in diabetic (db/db) mice with *Pseudomonas aeruginosa* biofilm challenge: A model for the study of chronic wounds. *Wound Repair Regen.* **18**, 467–477 (2010).
101. S. Singh, V. Rajagopal, N. Kour, M. Rao, R. Rao, I. Manipal, Platelet-rich plasma injection and becaplermin gel as effective dressing adjuvants for treating chronic nonhealing ulcers in patients with junctional epidermolysis bullosa. *J. Am. Acad. Dermatol.* **84**, e185–e186 (2021).
102. A. M. Tofigh, M. Tajik, Comparing the standard surgical dressing with dehydrated amnion and platelet-derived growth factor dressings in the healing rate of diabetic foot ulcer: A randomized clinical trial. *Diabetes Res. Clin. Pr.* **185**, 109775 (2022).
103. H. Yu, X. Chen, J. Cai, D. Ye, Y. Wu, L. Fan, P. Liu, Novel porous three-dimensional nanofibrous scaffolds for accelerating wound healing. *Chem. Eng. J.* **369**, 253–262 (2019).
104. G. Lu, Z. Ding, Y. Wei, X. Lu, Q. Lu, D. L. Kaplan, Anisotropic biomimetic silk scaffolds for improved cell migration and healing of skin wounds. *ACS Appl. Mater. Interfaces* **10**, 44314–44323 (2018).

105. X. Zhao, X. Sun, L. Yildirimer, Q. Lang, Z. Yuan, W. Lin, R. Zheng, Y. Zhang, W. Cui, N. Annabi, A. Khademhosseini, Cell infiltrative hydrogel fibrous scaffolds for accelerated wound healing. *Acta Biomater.* **49**, 66–77 (2017).
106. K. Nellenbach, S. Nandi, C. Peeler, A. Kyu, A. C. Brown, Neonatal fibrin scaffolds promote enhanced cell adhesion, migration, and wound healing in vivo compared to adult fibrin scaffolds. *Cell Mol. Bioeng.* **13**, 393–404 (2020).
107. I. Negut, G. Dorcioman, V. Grumezescu, Scaffolds for wound healing applications. *Polym.* **12**, 2010 (2020).
108. S. Park, D. G. Gonzalez, B. Guirao, J. D. Boucher, K. Cockburn, E. D. Marsh, K. R. Mesa, S. Brown, P. Rompolas, A. M. Haberman, Y. Bellaïche, V. Greco, Tissue-scale coordination of cellular behaviour promotes epidermal wound repair in live mice. *Nat. Cell Biol.* **19**, 155–163 (2017).
109. I. Pastar, O. Stojadinovic, N. C. Yin, H. Ramirez, A. G. Nusbaum, A. Sawaya, S. B. Patel, L. Khalid, R. R. Isseroff, M. Tomic-Canic, Epithelialization in wound healing: A comprehensive review. *Adv. Wound Care* **3**, 445–464 (2014).
110. R. B. Diller, A. J. Tabor, The role of the extracellular matrix (ECM) in wound healing: A review. *Biomimetics (Basel)* **7**, 87 (2022).
111. S. S. Mathew-Steiner, S. Roy, C. K. Sen, Collagen in wound healing. *Bioengineering* **8**, 63 (2021).
112. M. Zhao, H. Bai, E. Wang, J. V. Forrester, C. D. McCaig, Electrical stimulation directly induces pre-angiogenic responses in vascular endothelial cells by signaling through VEGF receptors. *J. Cell Sci.* **117**, 397–405 (2004).
113. S. Ud-Din, A. Sebastian, P. Giddings, J. Colthurst, S. Whiteside, J. Morris, R. Nuccitelli, C. Pullar, M. Baguneid, A. Bayat, Angiogenesis is induced and wound size is reduced by electrical stimulation in an acute wound healing model in human skin. *PLOS ONE* **10**, e0124502 (2015).
114. K. E. Johnson, T. A. Wilgus, Vascular endothelial growth factor and angiogenesis in the regulation of cutaneous wound repair. *Adv. Wound Care* **3**, 647–661 (2014).
115. G. J. Kotwal, S. Chien, Macrophage differentiation in normal and accelerated wound healing. *Results Probl. Cell Differ.* **62**, 353–364 (2017).
116. P. Krzyszczyk, R. Schloss, A. Palmer, F. Berthiaume, The role of macrophages in acute and chronic wound healing and interventions to promote pro-wound healing phenotypes. *Front. Physiol.* **9**, 419 (2018).
117. A. Sebastian, F. Syed, D. Perry, V. Balamurugan, J. Colthurst, I. H. Chaudhry, A. Bayat, Acceleration of cutaneous healing by electrical stimulation: Degenerate electrical waveform down-regulates inflammation, up-regulates angiogenesis and advances remodeling in temporal punch biopsies in a human volunteer study. *Wound Repair Regen.* **19**, 693–708 (2011).
118. I. Taskan, I. Ozyazgan, M. Tercan, H. Kardas, S. Balkanli, R. Saraymen, U. Zorlu, Y. Ozugul, A Comparative study of the effect of ultrasound and electrostimulation on wound healing in rats. *Plast. Reconstr. Surg.* **100**, 966–972 (1997).
119. J. D. Reich, A. L. Cazzaniga, P. M. Mertz, F. A. Kerdel, W. H. Eaglstein, The effect of electrical stimulation on the number of mast cells in healing wounds. *J. Am. Acad. Dermatol.* **25**, 40–46 (1991).
120. R. Zhao, H. Liang, E. Clarke, C. Jackson, M. Xue, Inflammation in chronic wounds. *Int. J. Mol. Sci.* **17**, 2085 (2016).
121. M. Li, Q. Hou, L. Zhong, Y. Zhao, X. Fu, Macrophage related chronic inflammation in non-healing wounds. *Front. Immunol.* **12**, 681710 (2021).
122. H. Derakhshandeh, F. Aghabaglou, A. McCarthy, A. Mostafavi, C. Wiseman, Z. Bonick, I. Ghanavati, S. Harris, C. Kreikemeier-Bower, S. M. M. Basri, J. Rosenbohm, R. Yang, P. Mostafalu, D. Orgill, A. Tamayol, A wirelessly controlled smart bandage with 3D-printed miniaturized needle arrays. *Adv. Funct. Mater.* **30**, 1905544 (2020).
123. M. Fu, Y. Zhao, Y. Wang, Y. Li, M. Wu, Q. Liu, Z. Hou, Z. Lu, K. Wu, J. Guo, On-demand removable self-healing and pH-responsive europium-releasing adhesive dressing enables inflammatory microenvironment modulation and angiogenesis for diabetic wound healing. *Small* **19**, e2205489 (2023).
124. M. R. Asadi, G. Torkaman, Bacterial inhibition by electrical stimulation. *Adv. Wound Care* **3**, 91–97 (2014).
125. R. Kirsner, C. Dove, A. Reyzelman, D. Vayser, H. Jaimes, A prospective, randomized, controlled clinical trial on the efficacy of a single-use negative pressure wound therapy system, compared to traditional negative pressure wound therapy in the treatment of chronic ulcers of the lower extremities. *Wound Repair Regen.* **27**, 519–529 (2019).
126. D. Schneider, B. Schultrich, Elastic modulus: A suitable quantity for characterization of thin films. *Surf. Coat. Technol.* **98**, 962–970 (1998).
127. S. J. Cho, K. R. Lee, K. Y. Eun, J. H. Hahn, D. H. Ko, Determination of elastic modulus and Poisson's ratio of diamond-like carbon films. *Thin Solid Films* **341**, 207–210 (1999).
128. C. Fuchs, L. Pham, J. Henderson, K. J. Stalnaker, R. R. Anderson, J. Tam, Multi-faceted enhancement of full-thickness skin wound healing by treatment with autologous micro skin tissue columns. *Sci. Rep.* **11**, 1688 (2021).
129. A. Mathis, P. Mamidanna, K. M. Cury, T. Abe, V. N. Murthy, M. W. Mathis, M. Bethge, DeepLabCut: Markerless pose estimation of user-defined body parts with deep learning. *Nat. Neurosci.* **21**, 1281–1289 (2018).
130. T. Nath, A. Mathis, A. C. Chen, A. Patel, M. Bethge, M. W. Mathis, Using DeepLabCut for 3D markerless pose estimation across species and behaviors. *Nat. Protoc.* **14**, 2152–2176 (2019).
131. S. G. Gürgen, O. Sayın, F. Çetin, A. Tuç Yücel, Transcutaneous electrical nerve stimulation (TENS) accelerates cutaneous wound healing and inhibits pro-inflammatory cytokines. *Inflammation* **37**, 775–784 (2014).
132. M. R. Asadi, G. Torkaman, M. Hedayati, M. Mofid, Role of sensory and motor intensity of electrical stimulation on fibroblastic growth factor-2 expression, inflammation, vascularization, and mechanical strength of full-thickness wounds. *J. Rehabil. Res. Dev.* **50**, 489–498 (2013).
133. P. Mostafalu, G. Kiaee, G. Giatsidis, A. Khalilpour, M. Nabavinia, M. R. Dokmeci, S. Sonkusale, D. P. Orgill, A. Tamayol, A. Khademhosseini, A textile dressing for temporal and dosage controlled drug delivery. *Adv. Funct. Mater.* **27**, 1702399 (2017).
134. J. Na, S. Y. Song, J. D. Kim, M. Han, J. S. Heo, C. E. Yang, H. O. Kim, D. H. Lew, E. Kim, Protein-engineered large area adipose-derived stem cell sheets for wound healing. *Sci. Rep.* **8**, 15869 (2018).

Acknowledgments: 3D-printed molds for creating dummy wounds were fabricated using 3D printers at the ASSIST Center at North Carolina State University which has received support from the National Science Foundation (EEC-1160483). **Funding:** This work was supported by Defense Advanced Research Projects Agency grant D20AC00004 (to M.A.J., D.G.K., E.A.C., G.T., B.J.S., A.V., and S.K.S.), North Carolina State University Start-up Grant (to A.J.B. and R.K.), Joint Department of Biomedical Engineering's REU program (to H.C.), and National Science Foundation grant EEC-1160483 (to H.C.). **Author contributions:** Conceptualization: R.K., M.A.J., A.J.B., and S.K.S. Methodology: R.K., M.A.J., B.J.S., G.T., and A.V. Software: R.K., M.A.J., B.E.U., W.B.H., T.-M.J., and S.-W.H. Investigation: R.K., M.A.J., D.G.K., E.A.C., H.C., B.J., N.M., and N.S. Visualization: R.K. and M.A.J. Supervision: A.J.B. and S.K.S. Writing—original draft: R.K., M.A.J., and A.J.B. Writing—review and editing: R.K., M.A.J., A.J.B., and S.K.S. **Competing interests:** A.J.B. and R.K. are inventors on a patent application related to this work filed by North Carolina State University, D2024-0114, filed 30 November 2023. The other authors declare that they have no competing interests. **Data and materials availability:** All data needed to evaluate the conclusions in the paper are present in the paper and/or the Supplementary Materials.

Submitted 19 February 2024
Accepted 28 June 2024
Published 7 August 2024
10.1126/sciadv.ado7538